

The cerebellum shapes motions by encoding motor frequencies with precision and cross-individual uniformity

Received: 21 June 2024

Accepted: 16 April 2025

Published online: 27 May 2025

 Check for updates

Chia-Wei Liu^{1,2,10}, Yi-Mei Wang^{2,3,10}, Shun-Ying Chen^{2,4,10},
Liang-Yin Lu^{2,4,10}, Ting-Yu Liang^{1,2}, Ke-Chu Fang^{1,2}, Peng Chen^{1,2}, I-Chen Lee^{1,2},
Wen-Chuan Liu^{1,2,5}, Ami Kumar^{6,7}, Sheng-Han Kuo^{6,7}, Jye-Chang Lee^{2,5},
Chung-Chuan Lo⁸, Shun-Chi Wu⁹ & Ming-Kai Pan^{1,2,3,4,5} ✉

Understanding brain behaviour encoding or designing neuroprosthetics requires identifying precise, consistent neural algorithms across individuals. However, cerebral microstructures and activities are individually variable, posing challenges for identifying precise codes. Here, despite cerebral variability, we report that the cerebellum shapes motor kinematics by encoding dynamic motor frequencies with remarkable numerical precision and cross-individual uniformity. Using *in vivo* electrophysiology and optogenetics in mice, we confirm that deep cerebellar neurons encode frequencies using populational tuning of neuronal firing probabilities, creating cerebellar oscillations and motions with matched frequencies. The mechanism is consistently presented in self-generated rhythmic and non-rhythmic motions triggered by a vibrational platform or skilled tongue movements of licking in all tested mice with cross-individual uniformity. The precision and uniformity allowed us to engineer complex motor kinematics with designed frequencies. We further validate the frequency-coding function of the human cerebellum using cerebellar electroencephalography recordings and alternating current stimulation during voluntary tapping tasks. Our findings reveal a cerebellar algorithm for motor kinematics with precision and uniformity, the mathematical foundation for a brain–computer interface for motor control.

Our brains control our decisions and behaviours with incredible precision and reliability, indicating existing neural algorithms for detailed behavioural control. Identifying such a precise algorithm for the human species requires precise coupling between neural activity and behaviours, not only valid in one person but consistent across individuals. However, cerebral microstructure and activity details are variable across individuals, even among identical twins¹. This variability poses major challenges in identifying reliable and precise neural codes necessary for understanding brain behavioural coding and

designing neuroprosthetics. Recent advances in deep learning have enabled the decoding of neuronal activity to behavioural outputs within a single subject². However, neural network variability prevents the transfer of a learned decoding model to a new subject without retraining on their specific neural-behavioural data, which is unavailable in patients who have lost related functions. Additionally, generative models have known reliability issues to create new behaviours beyond their training set, which is essential for generating a wide range of human behaviours. Identifying explainable and consistent neural

A full list of affiliations appears at the end of the paper. ✉ e-mail: emorymkpan@ntu.edu.tw

algorithms is a crucial scientific challenge and an unmet medical need for neuroprosthetic design.

In addition to the challenges posed by neural network variability among human brains, the spinal cords of different people and mice use the same neural mechanisms to control muscle activities with remarkable spatiotemporal precision. This consistency points to a specialized brain structure capable of translating high-dimensional conscious commands into temporally precise neural codes for motor kinematics. Recent studies suggest that the cerebellum plays a crucial role in linearly coding the kinematics. The cerebellum regulates the end-point precision of reach movement^{3,4}, motor-state changes of skilled movement⁵⁻⁷, eye saccades^{8,9}, tongue¹⁰ and harmaline-induced movements¹¹. The cerebellum is also adept at maintaining temporal accuracy¹², establishing specialized cortical connections¹³ and forming rapid olivocerebellar circuits¹⁴ for handling fast kinematics. The evidence suggests that our central nervous system may use the cerebellum as a linear encoder to build complex motor kinematics. However, individual variability remains an intrinsic feature of these time domain observations.

Fortunately, insights into human cerebellar disorders have shed light on the role of the cerebellum in motor kinematics coding. Cerebellar dysfunctions lead to the breakdown of motor kinematic control in a unique feature linked to motor frequencies. Essential tremor, the most common movement disorder, is characterized by involuntary rhythmic movements with a consistent motor frequency, linked to excessive cerebellar oscillations¹⁵⁻¹⁷. Conversely, cerebellar ataxia features arrhythmic involuntary movements that are associated with Purkinje cell (PC) loss^{18,19}. These abnormalities strongly suggest that cerebellar diseases have neuronal coding dysfunctions in forming motor frequencies.

Inspired by theories that subthreshold oscillations in the olivocerebellar circuits play a crucial role in motor control^{10,11,15-19}, this study investigates the potential of cerebellar frequency coding in shaping motor kinematics. We explored the frequency building blocks at both cellular and population levels and established that motor frequency coding is not only biologically robust, but also mathematically precise and generalizable. This suggests a cerebellar algorithm capable of creating complex motor kinematics with designed frequency dynamics.

Results

Cerebellar oscillatory frequencies report motor rhythms

Our initial investigations focused on whether the cerebellum encodes the motor frequencies of self-generated rhythmic movements in mice. To encourage the mice into generating motor behaviours at a predetermined frequency, we applied a horizontal vibrating platform that can vibrate at a specific fixed frequency or frequency as a function of time (Fig. 1a and Supplementary Video 1). Wild-type mice were trained to develop active motor compensation to the vibrations and could walk and stand freely on the platform (Supplementary Video 2). Self-generating motion can be calculated by subtracting the pre-designed sinusoidal platform vibrations from the head-mounted accelerometer signals, including both vibration and active motion (Fig. 1b). Both platform and head signals were detected simultaneously with accelerometers of the same design. When the mouse was at rest, the head moved with the platform, leading to similar waveforms of accelerometer signals from the head or the platform (Fig. 1b, grey). When the mouse performed compensatory movement to cancel out the platform vibrations, the head signals were dampened by motor compensation (Fig. 1b, orange, and Supplementary Video 2). The vibrations also allowed multiple muscles and joints to react at the same rhythm, which enhanced the frequency information across cerebellar topography. During 16 Hz platform vibrations, simultaneous local field potential (LFP) recordings from the cerebellar cortex revealed corresponding 16 Hz cerebellar oscillations (Fig. 1c-f). To rule out LFP artefacts generated by the vibration platform, we recorded hippocampal LFPs, which

displayed typical theta oscillations but no 16 Hz vibration-related signals (Supplementary Fig. 1). We also implanted electromyography (EMG) wires into the quadriceps muscles of the hindlimbs to validate active motor compensation. The EMG recordings confirmed active muscle contractions at the compensatory frequency in well-trained mice (Supplementary Fig. 2).

On the basis of this initial observation, we trained the mice with a protocol including multiple vibratory frequencies (Fig. 1g), covering the physiological frequency range of spontaneous motor behaviours¹⁶. We first performed a cross-correlation analysis between cerebellar LFPs and mouse motions (Fig. 1h). Compatible with previous knowledge, cerebellar signals are positively correlated with motions but with notable variation (Fig. 1i-m). However, it is possible that the cerebellum LFPs predominantly reflect the sensory inputs. We therefore cross-correlated cerebellar LFPs with accelerometer signals, which reflected overall motions and therefore corresponding overall sensory inputs. While the accelerometer signals also had strong frequency dependency (Fig. 1d), they were poorly correlated with cerebellar signals (Fig. 1k,m), suggesting a motor-predominant contribution of the cerebellar LFPs. The dynamics of cross-correlograms are highly variable across time and across individual mice (Fig. 1i-k), indicating a qualitative valid and quantitative imprecise scenario. In addition to the maximal cross-correlation, we further examined the detailed cross-correlation features across time shifts (Fig. 1n). Distinct periodic patterns emerged, each corresponding to a specific motor frequency. The frequency spectrum of the cross-correlation signals displayed a strong dependence on frequency, suggesting a potential mechanism for cerebellar frequency coding (Fig. 1o).

To explore the possibility of cerebellar frequency coding, we processed the LFP and motion signals in the frequency domain (Fig. 2a-d). The trained mice consistently generated movements at specific motor frequencies, with correspondingly enhanced cerebellar LFP amplitudes (Fig. 2c). While a general correlation was observed between motor activity and cerebellar LFP amplitudes on an individual basis, the increased LFP amplitudes varied across mice, preventing a precise correlation with motor amplitudes in a cross-individual analysis (Fig. 2e). In contrast, peak cerebellar oscillatory frequencies accurately encoded motor frequencies, demonstrating minimal individual variability and underscoring the potential role of the cerebellum in quantitative motor-rhythm coding (Fig. 2f).

The extracted frequency in Fig. 2f is the section-based average of frequency-dependent motions. If the cerebellum truly engages in the rhythm control of motor kinematics, the frequency coding should precisely reflect kinematic details. We performed a second-by-second analysis of all recordings, examining frequencies and amplitudes on a second-by-second basis (Fig. 2g,h). The cerebellar frequency consistently matched the motor frequency across all mice and throughout most of the 2,160 data points, highlighting a robust, quantitatively precise coding mechanism (Fig. 2g-j). By comparing the time and frequency domains, the imprecision of cerebellar kinematic coding is mainly contributed by the amplitude mismatches between cerebellar and motion signals (Fig. 2k). Next, we evaluated the interposed nucleus of the deep cerebellar nuclei (DCN), the output structure of the motor cerebellum^{3,4,17}. The DCN LFPs were significantly but variably correlated with the motor kinematics in the time domain (Supplementary Fig. 3), whereas LFP frequencies consistently matched motor frequencies across all examined mice and all 2,880 data points (Supplementary Fig. 4).

To determine whether the cerebellum can process multiple frequencies, we applied 13 Hz, 20 Hz or a combination of 13 Hz and 20 Hz vibrations to train compensatory motion. The mouse cerebellum reliably generated dual frequencies corresponding to the motor kinematics (Supplementary Fig. 5).

In summary, the cerebellum accurately encodes motor frequencies during self-generated rhythmic movements in mice, with minimal

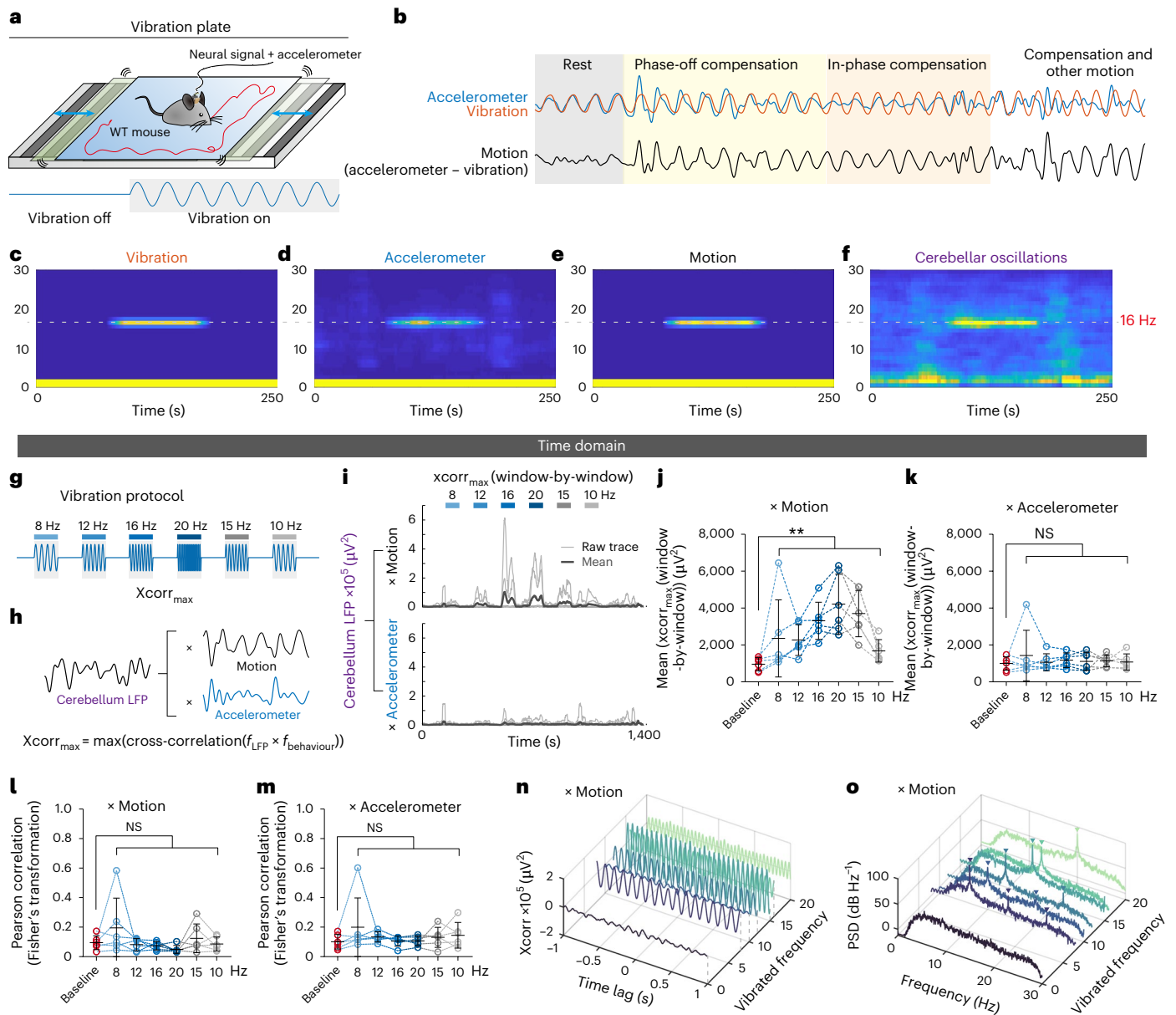


Fig. 1 | Self-generated cerebellar oscillations in compensatory motions. **a**, An experimental setting of the vibration platform generating horizontal sinusoidal motions. **b**, Representative traces for active compensatory motion, calculated as signals of a head-mounted accelerometer minus the platform vibrations. **c–f**, Representative time–frequency plots of vibrations (**c**), head-mounted accelerometer signals (**d**), compensatory motions (**e**) and cerebellar oscillations (**f**) during 16 Hz vibrations. **g**, A schematic of the vibration protocol, indicating the sequence of applied frequencies. $xcorr_{max}$, maximal cross-correlation. **h**, An illustration of the $xcorr_{max}$ for cerebellar LFPs with compensatory motions and residual body movements (accelerometer). **i**, A trial-by-trial profile of the $xcorr_{max}$ between cerebellar oscillations and compensatory motion (top) or accelerometer signals (bottom). **j–m**, The mean $xcorr_{max}$ values (**j** and **k**) and

Pearson correlation with Fisher’s transformation (**l** and **m**) between cerebellar oscillations and compensatory motion (**j** and **l**) or accelerometer (**k** and **m**) signals across various vibration frequencies. The statistical analysis in **j** was performed using the Friedman test; Friedman statistic of 26.93, $P = 0.0001$ (two sided). **n**, A three-dimensional plot of cross-correlation between cerebellar oscillations and compensatory motion, with the x axis representing the time lag, the y axis showing the vibration frequency and the z axis indicating cross-correlation values. **o**, A three-dimensional power spectral density (PSD) plot of the cross-correlation spectrum between cerebellar oscillations and compensatory motion, with the x axis indicating frequency, the y axis showing the vibration frequency and the z axis representing spectral power ($n = 6$ mice). Data are presented as mean values \pm s.d. NS, not significant. $**P < 0.01$.

individual variability. The cerebellar-encoded frequency (f), whether derived from the DCN or cerebellar LFPs, is equal to the motor frequency: $f_{cerebellar} = f_{motor}$

Population activity of DCN neurons encodes motor frequencies LFPs are the spatiotemporal summation of neuronal signals. We need to understand the building blocks at the single-cell level. To understand these signals at the single-cell level, we simultaneously recorded

single-unit (SU) activities and LFPs from the interposed nuclei of the DCN and analysed the corresponding motor kinematics in freely moving mice (Fig. 3a,b and Supplementary Figs. 6 and 7). We first evaluated whether DCN neuronal firing rates can represent motor frequencies. The motor frequencies were poorly correlated with neuronal firing rates, burst rates or their mean firing rates (Fig. 3c), against a simple rate-coding algorithm. We next evaluated whether the changes in firing probability, instead of the firing rate itself, could have a tuning

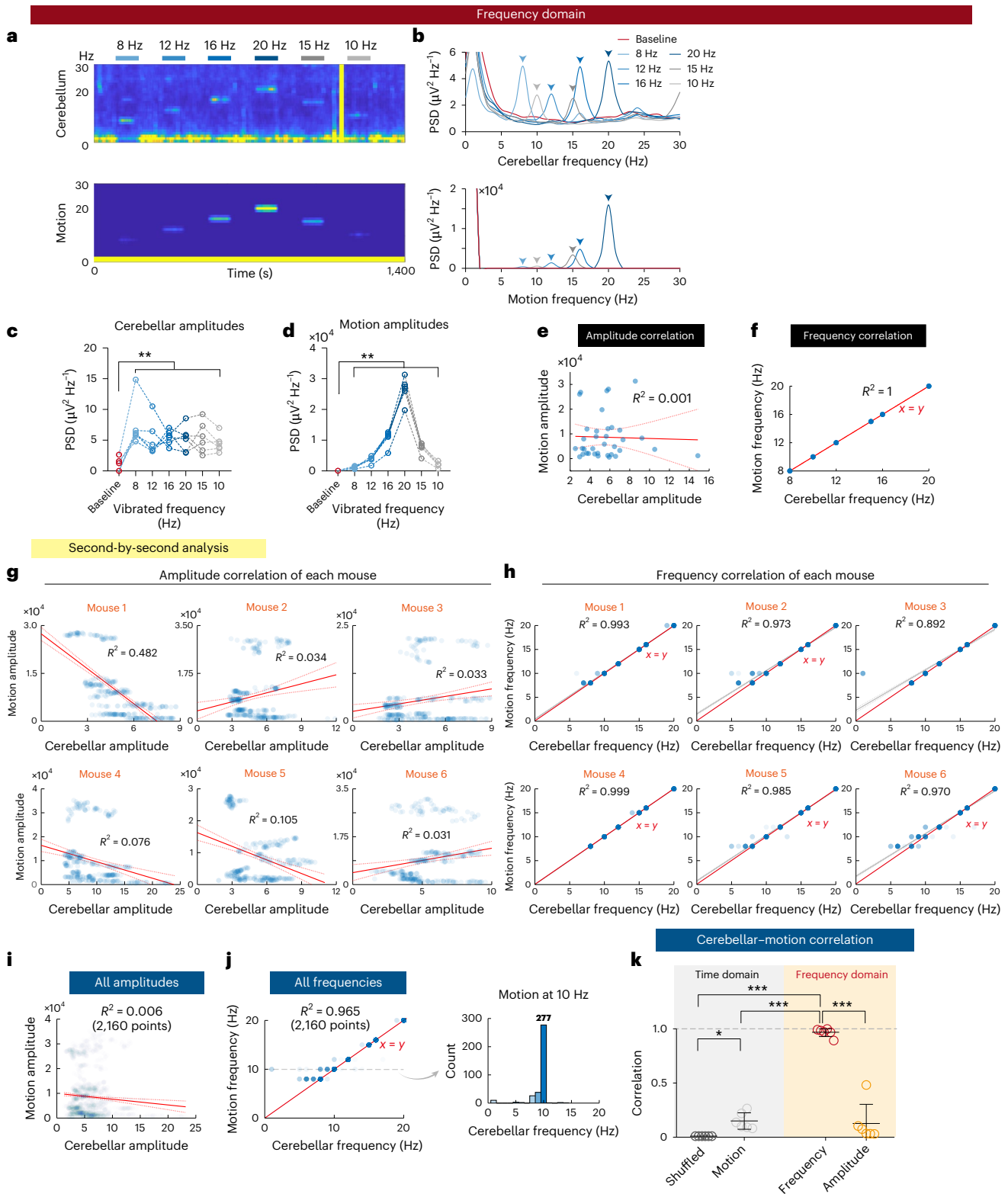


Fig. 2 | Correlation of cerebellar oscillations and rhythmic motions in the frequency domain. **a, b**, Representative time–frequency plots (**a**) and PSDs (**b**) across various vibrating frequencies. **c, d**, Peak PSD amplitudes of cerebellar oscillations (Friedman statistic of 18.14, $P = 0.0059$ (two sided)) (**c**) and compensatory motions (Friedman statistic of 36, $P < 0.0001$ (two sided)) (**d**) across various vibrating frequencies. **e**, A linear regression analysis of peak PSD amplitudes between cerebellar oscillations and compensatory motor movements. The solid red line represents the best-fit linear model, while the dashed red lines indicate the 95% confidence bounds (36 points in 6 mice). **f**, A linear regression analysis of the frequencies at peak PSD amplitudes for

cerebellar oscillations and motor activities (36 points in 6 mice). **g, h**, A second-by-second linear regression analysis of the amplitude correlation (**g**) and frequency correlation (**h**) for each mouse (360 points in each mouse). **i, j**, The collective second-by-second analysis for all amplitudes (**i**) and all frequencies (**j**) in all mice combined (2,160 points in 6 mice). **k**, Statistical analysis of the correlation between cerebellar LFPs and motor activity in both the time domain and the frequency domain, using Pearson correlation with Fisher’s transformation and the determination coefficient (R^2) of the linear regression presented in **i** and **j**, respectively ($n = 6$ mice, one-way ANOVA; $F = 111.9$, $P < 0.0001$). Data are presented as mean values \pm s.d. * $P < 0.05$, ** $P < 0.01$ and *** $P < 0.001$.

periodicity to represent motor frequencies. We leveraged vector strength spectrum analysis^{20–24}, a mathematical method using frequency vectors to unbiasedly extract probability tuning strength across frequencies (Fig. 3d). The vector strength frequencies were highly variable at the single-cell level (Fig. 3e). However, a specific frequency emerged with improving prominence when more and more neurons were included (Fig. 3f). This populationally encoded frequency converged towards the matched DCN oscillatory frequency and motor frequency with the same numerical value (Fig. 3g,h), with increasing signal-to-noise ratio (SNR) during the expansion of population size (Fig. 3i). This population-coding mechanism remained valid across all tested frequencies (Supplementary Fig. 8). Next, we applied autocorrelation to explore the intrinsic tuning of neuronal firing probabilities (Fig. 3j–n). Similar to the results of the vector strength analysis, the autocorrelogram did not generate consistent tuning frequency at the single-cell level but faithfully reported the motor frequencies at the populational level (Fig. 3j–n and Supplementary Fig. 9).

If the DCN neurons contribute to the generation of motor frequencies, the neuronal firing times should not be random but periodically tuned to the phases of the frequency-dependent motor kinematics. To validate the prediction, we extracted the instantaneous phases of motor kinematics based on the neuronal firing times (Fig. 3o) and quantified the phasic bias by polarity index, a numerical index ranging from 0 (purely random firings) to 1 (complete phase-locked firings)¹⁵. While some units exhibited higher polarity when compared with the shuffled data (Fig. 3p,q), all units have relatively low polarity index (<0.4) (Fig. 3r); therefore, no single neuron can explain the precise frequency coding of motor kinematics. Notably, phase biases of neuronal firings were significantly higher than the random process at the populational level (Fig. 3r,s and Supplementary Figs. 10 and 11). Direct visualization of simultaneously recorded SUs also supported the prediction of the abovementioned frequency and phase analysis at the populational level (Supplementary Fig. 12).

Taken together, the DCN neurons encode the frequencies of motor kinematics throughout population coding. While each neuron generates noisy or stochastic signals, the neuronal population achieves a high SNR and precise frequency coding. This confirms that LFPs, as spatiotemporal summations of these population activities, accurately reflected the synchronized frequencies between neuronal codes, LFPs and motor kinematics.

Rhythmic DCN stimulation induces motor rhythms

To establish the causality of the frequency-coding mechanism in motor kinematics, we optogenetically stimulated DCN neurons in

Thy1:ChR2-EYFP mice and recorded the resultant motor kinematics using a pressure-sensing force plate^{15,16} (Fig. 4a). Rhythmic stimulation led to a periodic increase in neuronal firings (Fig. 4b). Consistently, the SU-firing rates were way above the motor frequencies (Fig. 4c), against the rate-coding algorithm. Instead, the rhythmic optogenetic stimulation generated motor rhythm at the stimulating frequencies, and the populational tuning frequencies precisely converged to the motor frequencies at all tested scenarios (Fig. 4d–h). Phase analysis further verified the consistent feature of population coding at all stimulating frequencies (Supplementary Fig. 13).

We also evaluated cerebellar LFPs simultaneously recorded with the motor kinematics (Fig. 4i,j). The optogenetic stimulation led to increased but varied amplitudes of cerebellar oscillatory strengths and motor rhythms (Fig. 4k,l). In contrast, cerebellar and motor frequencies were always matched (Fig. 4m). The second-by-second analysis revealed amplitude variations across time and individuals, while the oscillatory and induced motor frequencies were always matched (Fig. 4n). Comparison between time and frequency domains confirmed that amplitude variability contributed to the imprecise cerebellar coding of rhythmic movements, while frequency information remained numerically precise (Fig. 4o).

Next, we investigated the laterality of DCN-encoded motor rhythms. Using video recordings of the mouse limbs, we observed ipsilateral limb movements induced by rhythmic optogenetic stimulation (Supplementary Fig. 14 and Supplementary Video 4). These results suggest the presence of laterality in the frequency coding of limb movements.

To further confirm the specificity of DCN-mediated motion generation, we virally transfected hSyn-ChR2-EYFP into the interposed nucleus of the DCN in wild-type (WT) mice (Supplementary Fig. 15). Optogenetic activation of these transfected DCN neurons successfully generated rhythmic motions corresponding to each stimulation frequency. We also investigated the role of motor amplitude tuning by rhythmically stimulating the DCN with varying light intensities (Supplementary Fig. 16). Consistent with cerebellar recordings during voluntary movements, which showed significant amplitude tuning properties (Fig. 2d and Supplementary Fig. 4d), increased light intensity produced stronger rhythmic motions (Supplementary Fig. 16a–e). However, analyses on a second-by-second basis and across entire periods revealed substantial variations (Supplementary Fig. 16f,g), indicating less precise amplitude coding. The correlation slopes between motion amplitude and cerebellar activity varied among individual mice, suppressing the overall cross-individual correlation (Supplementary Fig. 16h,i) and failing to provide the cross-individual uniformity

Fig. 3 | Neuronal coding for rhythmic motions. **a**, A scheme of simultaneous recordings of SU neuronal activities, DCN LFPs and motion kinematics. **b**, A representative plot of the optotrode trajectory labelled with Dil (a representative image of one mouse; eight mice were recruited for analysis with matched cannula trajectory; Methods). **c**, The SU-firing rates (grey circles) and burst rates (orange circles) in DCN versus motion frequencies ($n = 222$ units from 8 mice). **d**, A scheme of the vector strength spectrum analysis. **e**, Vector strengths of ten SUs. **f**, Frequency convergence of the vector strength of a representative trial during 16 Hz vibration. The vector strength spectrum peaks converged to the motion frequency throughout the random selection of included units. Intensity is in arbitrary units of vector strength (no unit), LFPs or motions (mV). The blue spectrum represents the mean vector strength of included units, the black spectrum represents the DCN LFP and the purple spectrum represents the motion. **g**, Frequency convergence of motions, LFPs and vector strength data superimposed in all trials of all mice. The top two subplots show the frequency spectrum of motion (top) and cerebellar LFP (middle). The light lines represent single trials and the heavy lines represent the averages of all trials. All peaks with sufficient prominence (Methods) detected in the vector strength spectrums throughout the expansion of the unit population (bottom). The colour gradient from green to blue reflects increasing units to calculate the vector strength spectrum. The colour depth indicates the level of prominence ($n = 138$ units

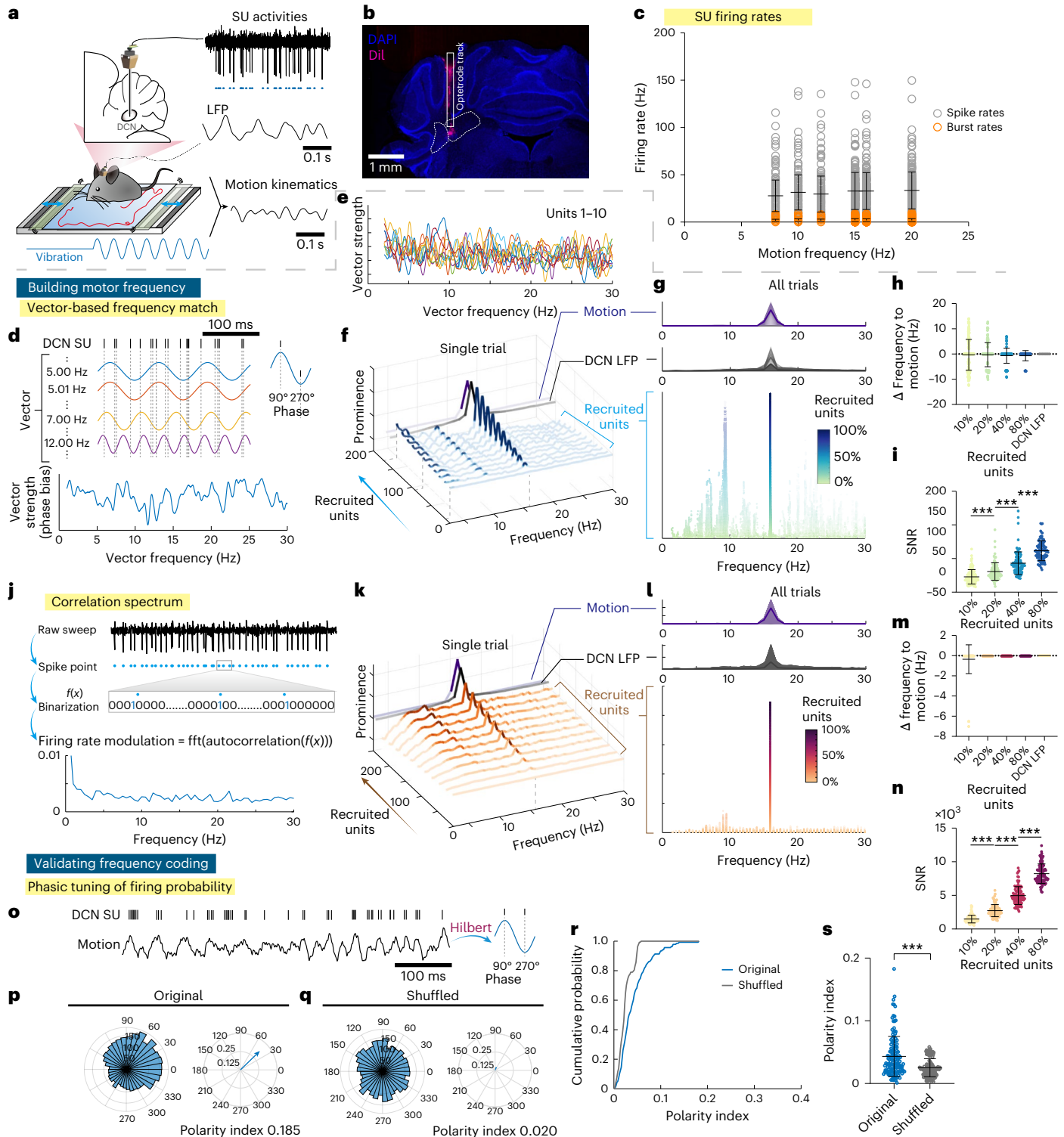
from 8 mice). Units with a minimum spike number <10 were excluded to avoid unreliable computation of vector strength). **h,i**, Quantitative analysis of vector strength spectrums: the peak frequency differences to motions (**h**) from vector strength spectrum (left four, green to blue) or from DCN LFPs (rightmost, grey) and the SNR (**i**) (Friedman statistic of 213.3, $P < 0.0001$ (two sided)), indicating peak prominence of corresponding vector strength spectrums ($n = 138$ units from 8 mice). **j–n**, The tuning frequencies of neuronal firing probabilities via autocorrelation spectrum (**j**) with a representative trial (**k**), group analysis (**l**) and quantification (Δ frequency to motion (**m**) and SNR (**n**), $n = 138$ units from 8 mice; Friedman statistic of 292.9, $P < 0.0001$ (two sided)). **o**, A scheme of the phasic tuning of SU-firing probabilities to the instantaneous phases of motion. **p,q**, Representative polar plots for original (**p**) and shuffled (**q**) data. DCN neurons had a greater phasic bias to the phase of motion, quantified by the polarity index. **r,s**, Group analysis of cumulative probabilities (**r**) and values (**s**) of polarity indexes. DCN neurons revealed stronger phasic tuning to 16 Hz compensatory motion at the populational level ($n = 138$ units from 8 mice, Wilcoxon matched-pairs signed-rank test; $W = -6,691$, $P < 0.0001$, two sided). See Methods for detailed definitions of burst detection, vector strength and peak prominence. Data are presented as mean values \pm s.d. Units represent biologically independent recordings from different neurons. *** $P < 0.001$.

required for precise engineering as seen in frequency coding (Fig. 4 and Supplementary Fig. 15).

A strong phase relationship between DCN firings and cerebellar LFPs indicated potential circuitry interactions between the cerebellar cortex and DCN (Supplementary Fig. 17). We also explored the role of axonal projections from PCs to DCN in this frequency-coding process (Supplementary Fig. 18). Rhythmic stimulation of PC axonal terminals generated rhythmic motions at the stimulating frequencies with matched population-coding mechanism, phase population effect and cerebellar oscillations across all tested mice (Supplementary Figs. 18–20).

We also performed computational modelling of noisy DCN neurons with the baseline firing rates at 20–22 Hz. When receiving inhibitory inputs of PCs at the frequency of 16 Hz, the populational tuning frequency converged to 16 Hz, while the mean firing rates stayed the same (Supplementary Fig. 21). This supports the experimental data, indicating that DCN neurons can adapt their population tuning frequencies by PCs to encode motor frequencies without substantial changes of their intrinsic firing properties.

Taken together, frequencies encoded by populations of DCN neurons can produce corresponding motor frequencies. The cerebellar cortex regulates DCN frequency codes through PC-to-DCN modulation.



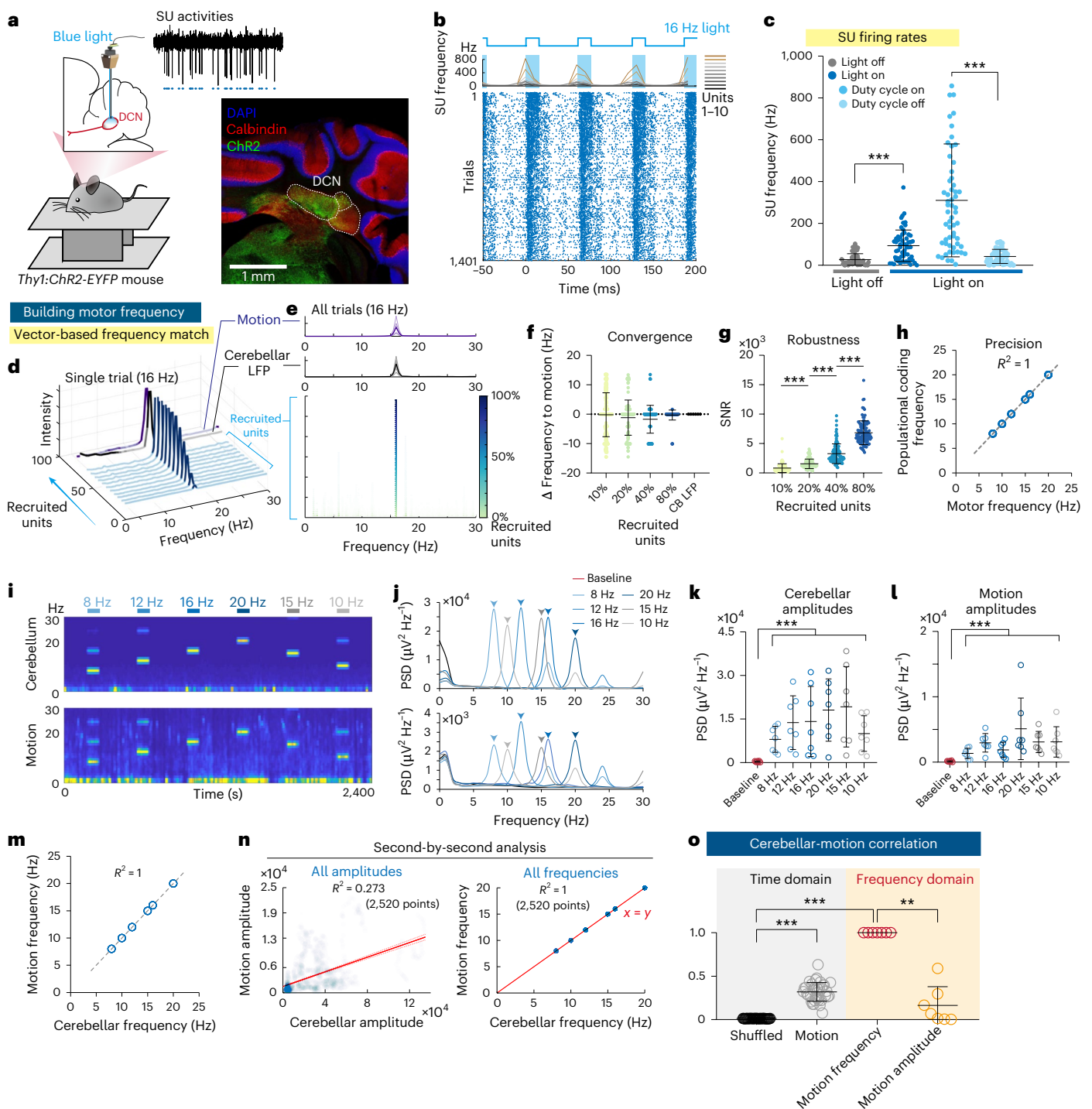


Fig. 4 | Cerebellar and motor responses to optogenetic DCN stimulation at multiple frequencies. **a**, A schematic of the experimental set up and representative histology of channelrhodopsin-2 (ChR2)-expressing DCN. **b**, Representative traces showing SU-firing rates (top) and their modulation during 16 Hz optogenetic stimulation of the DCN (bottom). **c**, Statistical analysis of SU-firing rates across different phases of the 16 Hz stimulation cycle ($n = 58$ units from 6 trials in 2 mice, one-way ANOVA; $F = 62.56$, $P < 0.0001$). **d–g**, Vector strength analysis, including a representative example (**d**), group analysis (**e**), frequency differences between motion and vector strength group spectrum peaks (**f**) and SNR of the spectrum peaks (**g**) ($n = 58$ units from 6 trials in 2 mice, one-way ANOVA; $F = 208.2$, $P < 0.0001$). CB, cerebellar. **h**, A scatter plot of the peak cerebellar LFP frequencies against combined vector strength spectrum peaks under various stimulating frequencies. **i, j**, Representative time-frequency plots (**i**) and spectral diagrams (**j**) of optogenetically driven cerebellar

oscillations and corresponding motor activities. **k–m**, Peak PSD amplitudes of cerebellar oscillations (Friedman statistic of 25.22, $P = 0.0003$ (two sided)) (**k**) and motions (Friedman statistic of 28.90, $P < 0.0001$ (two sided)) (**l**) across various stimulating frequencies. Collective data from seven trials in three mice showing the close correspondence between cerebellar oscillatory and motor frequencies (**m**). **n**, Scatter plots of the amplitudes (left) and frequencies (right) of cerebellar LFPs and motor activity, compiled from 1 s intervals across all trials (2,520 points from 7 trials in 3 mice). **o**, Statistical analysis of the Pearson correlation with Fisher's transformation between cerebellar LFPs and motor activity in the time domain and the determination coefficient (R^2) of the linear regression presented in **n** (from 7 trials in 3 mice, Kruskal–Wallis test, Kruskal–Wallis statistic of 63.12, $P < 0.0001$, two sided). Data are presented as mean values \pm s.d. Units represent biologically independent recordings from different neurons. ****** $P < 0.01$ and ******* $P < 0.001$.

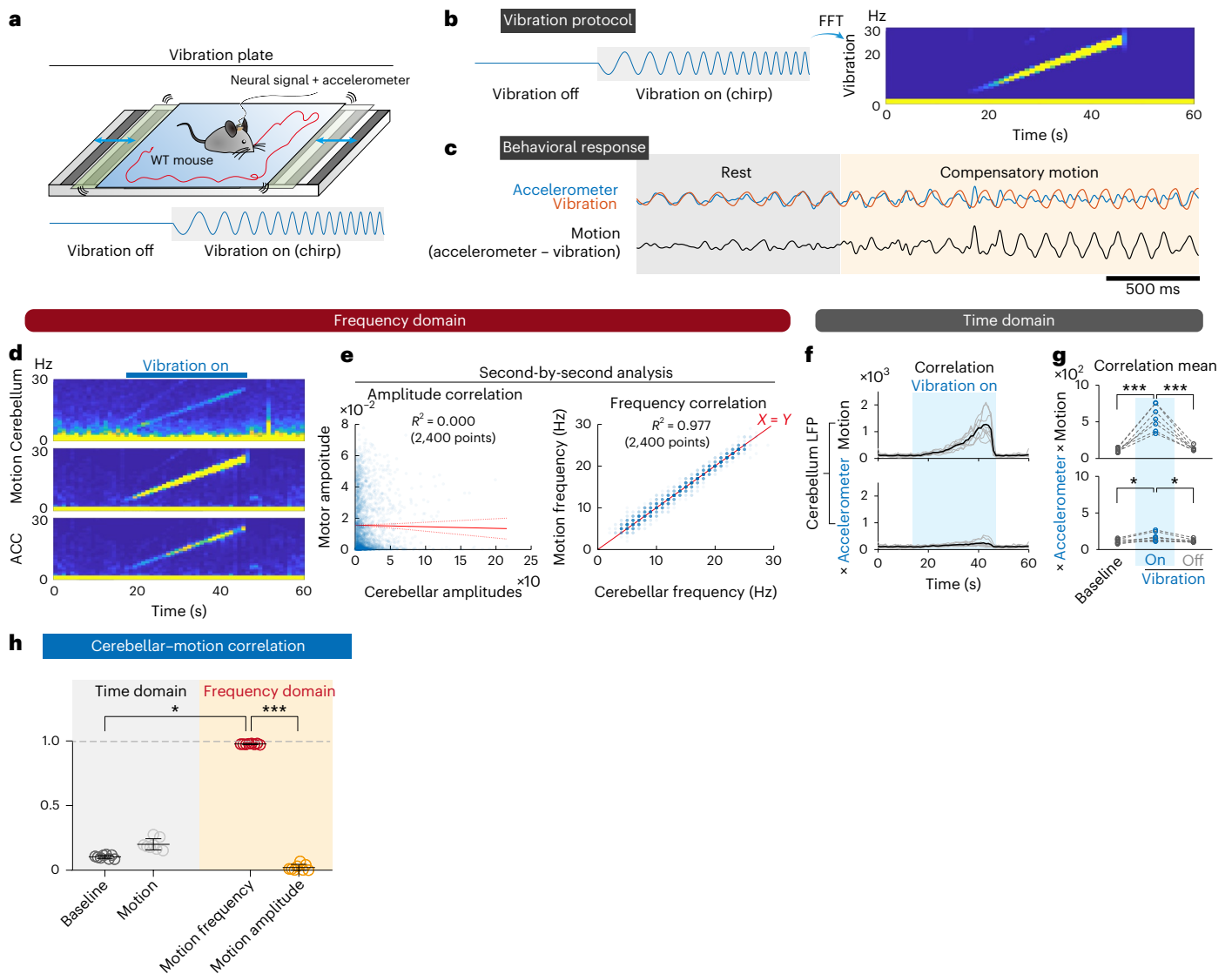


Fig. 5 | Non-rhythmic cerebellar oscillations and motor kinematics induced by linear chirp vibrations. **a**, The experimental settings and platform vibrations with constantly changing chirp waveform. **b**, A schematic representation of vibration protocol and the time–frequency plot of the vibration signals. **c**, Representative traces for compensatory motions. **d,e**, Frequency domain analysis: a representative time–frequency plot of cerebellar LFPs, motions and accelerometer signals (ACC) (**d**) and linear regression analysis of second-by-second amplitudes and frequencies between the cerebellar LFPs and motions (**e**)

(2,400 points from 80 trials in 8 mice). **f,g**, Time domain analysis: trial-by-trial (**f**) and group analysis (**g**) of cross-correlation for cerebellar oscillations between compensatory motions and residual body movements (accelerometer; Friedman statistic of 9.75, $P = 0.0048$ (two sided)). **h**, Statistical analysis of the correlation between cerebellar oscillation and motion in both the time domain (Pearson correlation with Fisher's transformation) and the frequency domain (R^2) ($n = 8$ mice; Friedman statistic of 24, $P < 0.0001$ (two sided)). Data are presented as mean values \pm s.d. * $P < 0.05$ and *** $P < 0.001$.

While optogenetic stimulation of the DCN supports the role of the cerebellum in the amplitude coding of movements, it does so with less precision and notable cross-individual variability.

Cerebellar dynamic frequencies encode non-rhythmic movement

While previous results detailed the cerebellum's encoding of rhythmic movements, most everyday movements are non-rhythmic. Theoretically, any finite signal, whether rhythmic or not, can be fully represented and reconstructed in the frequency domain. Non-rhythmic signals can be constructed using dynamically changing instantaneous phases/frequencies and amplitudes (via Hilbert transform) or multiple sets of these components in linear combinations (via Hilbert–Huang transform). Therefore, if the cerebellum can generate highly dynamic frequencies across time, it has the potential

to create non-rhythmic complex motor kinematics with the same frequency-coding mechanism.

To explore this hypothesis, we introduced floor vibrations with a linear chirp waveform to mice—a complex, non-rhythmic waveform characterized by constantly changing frequencies in a designed linear trend (Fig. 5a–c and Supplementary Video 3). This waveform is a strictly non-rhythmic pattern in which the instantaneous frequencies at any two moments are different. Using a linear chirp vibration from 4 to 25 Hz in 30 s, the mouse cerebellum generated dynamic cerebellar oscillations and compensatory motions with matched frequency dynamics of the designed protocol (Fig. 5d,e). These self-generated cerebellar oscillations correlated strongly with compensatory motions but showed minimal correlation with residual body movements recorded by an accelerometer (Fig. 5f,g). Consistently, while frequency-dependent amplitudes of both cerebellar oscillations

and motions were significantly increased (Fig. 5d), the magnitudes of increment remained poorly correlated on second-by-second analysis, therefore prohibiting the precise amplitude coding of motor kinematics (Fig. 5h).

Next, we optogenetically illuminated the DCN with the same linear chirp in *Thy1:ChR2-EYFP* mice. Cerebellar oscillations can be reliably generated with precisely matched time–frequency dynamics. The mice developed complex motor kinematics with the motor frequencies that matched the cerebellar oscillatory frequencies at nearly every time point (Fig. 6a–d and Supplementary Video 5). Linear chirp illumination at DCN with virally transfected *hSyn-ChR2-EYFP* produced a similar effect (Supplementary Fig. 22). Analysis of DCN SU activities during chirp stimulation revealed a unique neuronal-firing pattern consistent with the prediction from stimulation dynamics (Fig. 6f–i and Supplementary Fig. 22). The ability of the neurons to follow these complex temporal dynamics supports their role in forming rapidly changing frequency dynamics. Consistently, the populational DCN firing probabilities were faithfully tuned to Hilbert-based instantaneous phases/frequencies, cerebellar LFPs and motion kinematics (Supplementary Fig. 23).

Besides linear chirp, we further pushed the complexity of frequency dynamics by optogenetically illuminating DCN with complex chirp waveforms (Fig. 6j,k). Like the simpler linear chirps, complex chirp illumination evoked corresponding dynamics of cerebellar oscillations (Fig. 6l–n) and neuronal firings (Fig. 6o–q), thus generating matched frequency dynamics of mouse motor kinematics. While we achieved frequency precision for simple or complex motor kinematics, the motor amplitudes remained imprecisely correlated (Fig. 6c,l). Therefore, this approach has yet to generate functional or skilled movements, which requires precise coding for both motor frequencies and amplitudes across all time points.

Taken together, the cerebellum encodes complex frequency dynamics that match motor kinematic frequencies in self-generated, non-rhythmic movements. Optogenetic stimulation confirmed that the cerebellum can causatively generate non-rhythmic motor kinematics by dynamically encoding motor frequencies. With the preserved algorithm and numerical precision of frequency coding across all tested mice, we can use optogenetics to create complex motor kinematics with designed motor frequencies. The cerebellar-encoded frequency over time matches with the motor frequency dynamics,

$$\text{Cerebellar}(f, t) = \text{Motor}(f, t).$$

Cerebellar frequency coding predicts skilled tongue movement

The vibration platform and force plate were designed to target global body motions involving multijoint synchrony. We aimed to determine whether the cerebellar frequency-coding algorithm could also predict more localized, skilled movements. To explore this, we investigated tongue movement during licking behaviours while simultaneously

recording electrophysiological data from the dentate nucleus of the DCN²⁵ (Supplementary Fig. 24a–c). Consistently, the frequencies of dentate LFPs were highly correlated with the licking rates (Supplementary Fig. 24d), and the SU activities were tuned with the dentate LFPs at the populational level (Supplementary Fig. 24e–h). Notably, recordings from the interposed nucleus also provided precise frequency codes (Supplementary Fig. 24i–o), suggesting that both the interposed and dentate nuclei contribute to lick frequency coding.

Taken together, the cerebellum encodes frequency dynamics for complex motor kinematics, which is evident in global body movements and skilled tongue movements.

The human cerebellum engages in rhythm control of movement

To examine whether the human cerebellum also engages in frequency control of volitional movements, we analysed cerebellar electroencephalogram (EEG) and corresponding surface EMG signals of healthy subjects performing rhythmic tapping at 4, 5 and 6 Hz (Fig. 7a,b and Supplementary Table 1). Mirroring our findings in mice, cerebellar oscillations were detected during finger tapping, closely matching the EMG signal frequencies in a second-by-second analysis across individuals (Fig. 7c–f). The spatial map of frequency-dependent EEG signals revealed greater cerebellar than occipital power at the tapping frequencies (Supplementary Fig. 25), indicating that these activities originated from the cerebellum rather than from volume conduction artefacts in the sensorimotor cortices, which would have produced greater occipital power.

To probe the causal role of frequency coding in the human cerebellum, we employed transcranial alternating current stimulation (tACS) to modulate cerebellar oscillations. Using strong currents to modify the frequency of cerebellar oscillations may be dangerous. Therefore, we evaluated the frequency stability of motions by applying 4 Hz tACS to healthy subjects during 4 Hz finger tapping (Fig. 7g–i and Supplementary Table 1). Similar to the effects of bidirectional modulations of tremor amplitudes by cerebellar tACS²⁶, in-phase or anti-phase stimulation may bidirectionally change the stability of motor rhythms. We utilized a 4 Hz click sound to aid subjects in adjusting their tapping frequencies and recorded accelerometer-based kinematics during both sound-on and sound-off periods. The amplitude-independent kinematics were extracted to evaluate frequency stability (Methods). During the sound-off periods, tACS was found to either increase or decrease tapping frequency stability (Fig. 7j), demonstrating effective frequency modulation. During the sound-on period, the tapping kinematics were tightly guided by the sound, therefore revealing a better correlation to the 4 Hz waveforms without a difference to tACS manipulation (Fig. 7k,l).

Taken together, the cerebellar circuit of the healthy subjects also actively engages in frequency coding of volitional movements. Manipulation of cerebellar oscillations could enhance or suppress the frequency stability of motor rhythms.

Fig. 6 | Non-rhythmic cerebellar oscillations and motor kinematics induced by optogenetic stimulation. **a**, Optogenetic DCN stimulation with linear chirp waveform. **b**, A representative time–frequency plot of stimulating signals, cerebellar LFPs and motions. **c**, Frequency domain analysis, linear regression analysis of second-by-second amplitudes and frequencies between the cerebellar LFPs and motions (239 points in 8 mice). **d**, Time domain analysis. Trial-by-trial (left) and group analysis (right) of cross-correlation for cerebellar LFPs between motions (Friedman statistic of 12, $P = 0.0011$ (two sided)). **e**, Statistical analysis of the correlation between cerebellar oscillations and motions in both the time domain (Pearson correlation) and frequency domain (R^2) ($n = 8$ mice; Friedman statistic of 22.2, $P < 0.0001$ (two sided)). **f**, SU activities of DCN with linear chirp-wave stimulation. **g**, Predicted chirp points of maximal firing probability and their evolution across stimulation trials (defined by the number of peaks of chirp waves). **h**, The activity evolution of a representative SU. **i**, A group analysis

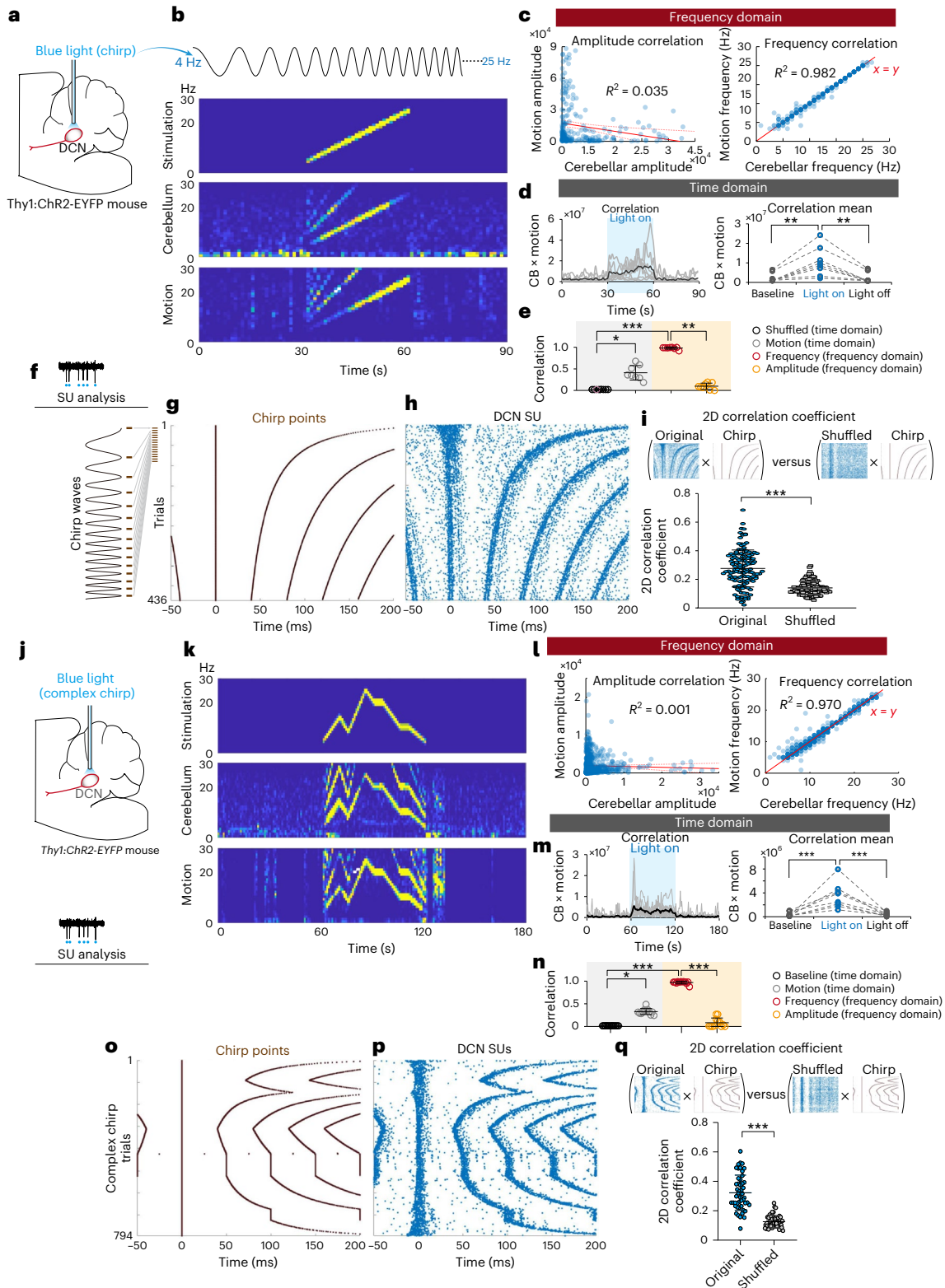
of correlation coefficient of DCN firings and chirp waveforms ($n = 136$ units from 8 mice, Wilcoxon matched-pairs signed-rank test; $W = -9,018$, $P < 0.0001$, two sided). **j**, Replication of the experiment with a complex chirp waveform stimulation. **k**, A representative time-frequency plots of the stimulation signal, cerebellar LFPs and motions. **l**, Frequency domain analysis (710 points in 12 mice). **m**, Time domain analysis (Friedman statistic of 18.17, $P < 0.0001$ (two-sided)). **n**, Statistical analysis (Friedman statistic of 32.4, $P < 0.0001$ (two-sided)). **o**, Predicted chirp points of maximal firing probability and their evolution across stimulation trials. **p**, The activity evolution of a representative SU. **q**, Group analysis of correlation coefficient of DCN firing and chirp waveforms (48 units in 12 mice; Wilcoxon matched-pairs signed-rank test; $W = -1,172$, $P < 0.0001$, two sided). Data are presented as mean values \pm s.d. * $P < 0.05$, ** $P < 0.01$ and *** $P < 0.001$. CB, cerebellum.

Discussion

In this study, we provided mouse evidence and supporting human evidence that the cerebellum encodes motor frequencies for physiological motor kinematics. The frequency is encoded by the integrative phasic tuning of neuronal firing probabilities at the populational level. While the motor amplitudes are highly variable and contribute to the variability of cerebellar kinematic coding in the time domain, the cerebellum encodes motor frequency with quantitative precision and generalizability across individuals without the need for additional calibration.

This level of precision allows us to engineer frequency dynamics for complex motor kinematics in mice. Among many cerebellar functions, cerebellar rhythm coding emerges as a numerically precise and generalizable algorithm, potentially serving as a mathematical backbone for future quantitative studies of neural dynamics. The key features of frequency coding are summarized in Fig. 8.

There are limitations in this study. First, the study design did not include topographical information about different muscle groups, which have been described in the cerebellum^{3,27}. We applied a vibration



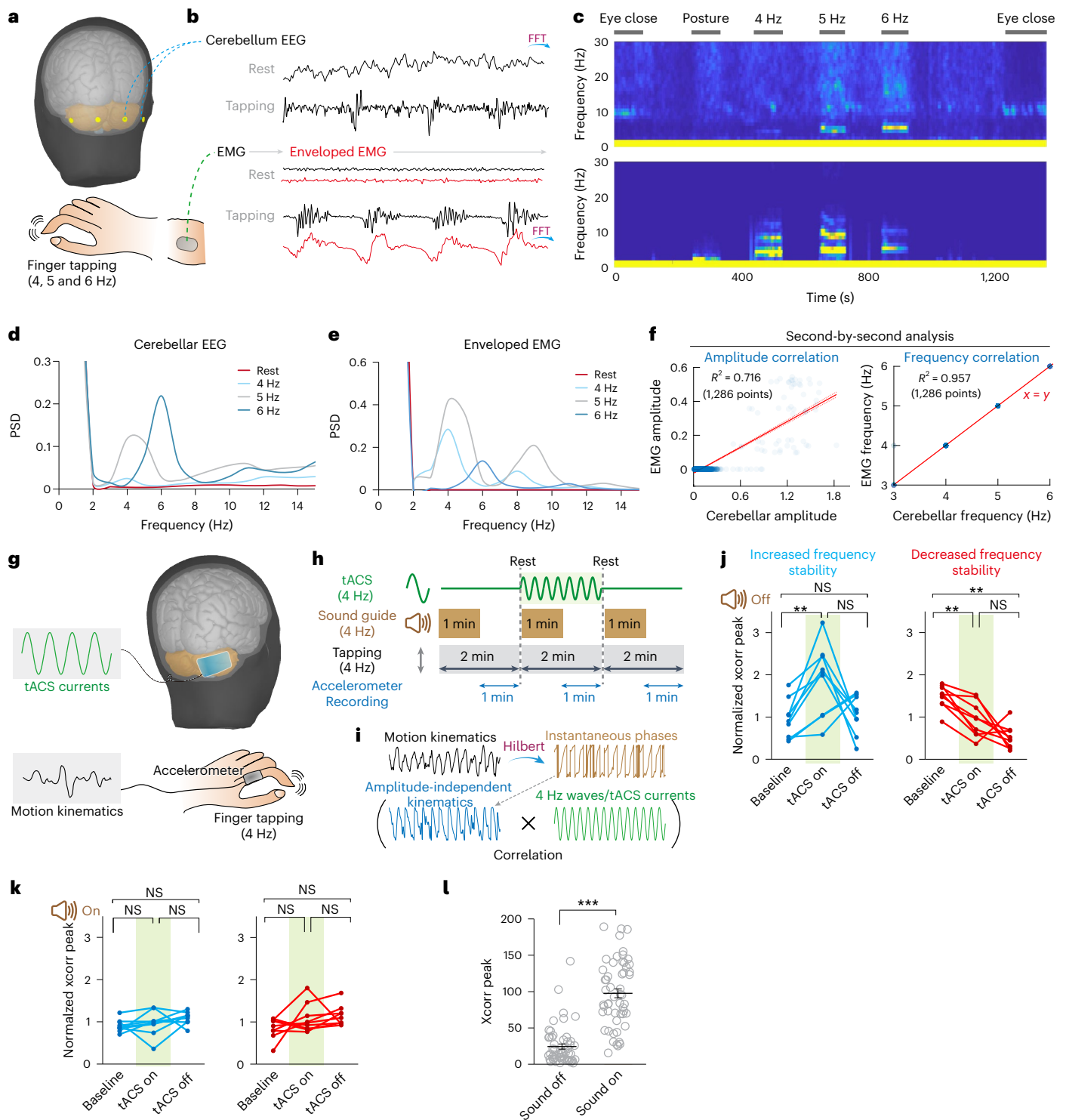


Fig. 7 | Cerebellar oscillations and their frequency modulation during volitional tapping of healthy subjects. **a**, Experimental settings of cerebellar EEG and EMG. **b–e**, Representative traces (**b**), time–frequency plots (**c**) and spectral diagrams of cerebellar EEG (**d**) and EMG (**e**). **f**, Linear regression analysis of second-by-second amplitudes and frequencies of cerebellar oscillations and EMG activities at the tapping frequencies (1,286 points, $n = 10$ subjects). **g**, Cerebellar tACS and simultaneous recording of tapping kinematics. **h**, The study protocol. tACS was set at the tapping frequency of 4 Hz and applied during the middle 2 min of volitional tapping. **i**, Frequency stability calculated from amplitude-independent kinematics (Methods). **j**, tACS modulation of the frequency stability of motion kinematics without a sound guide. Bidirectional

modulation was observed ($n = 6$ subjects with 3 repeated experiments; 9 and 9 trials with increased and decreased of frequency stability, respectively). Wilcoxon signed-rank test (two sided). Increased group: $P = 0.0039$ (baseline versus on), 0.0547 (on versus off) and 0.6523 (baseline versus off); decreased group: $P = 0.0039$, 0.0742 and 0.0078, respectively. **k**, tACS modulation of the frequency stability of motion kinematics with a sound guide. No significant modulation was observed. **l**, Cross-correlation (xcorr) peaks between tapping kinematics and tACS waveform. Values in the sound-on period were significantly higher than the sound-off period (the same 18 trials in 6 subjects, Wilcoxon signed-rank test; $W = 1,326$, $P < 0.0001$, two sided). Data are presented as mean values \pm s.e.m. ****** $P < 0.01$ and ******* $P < 0.001$.

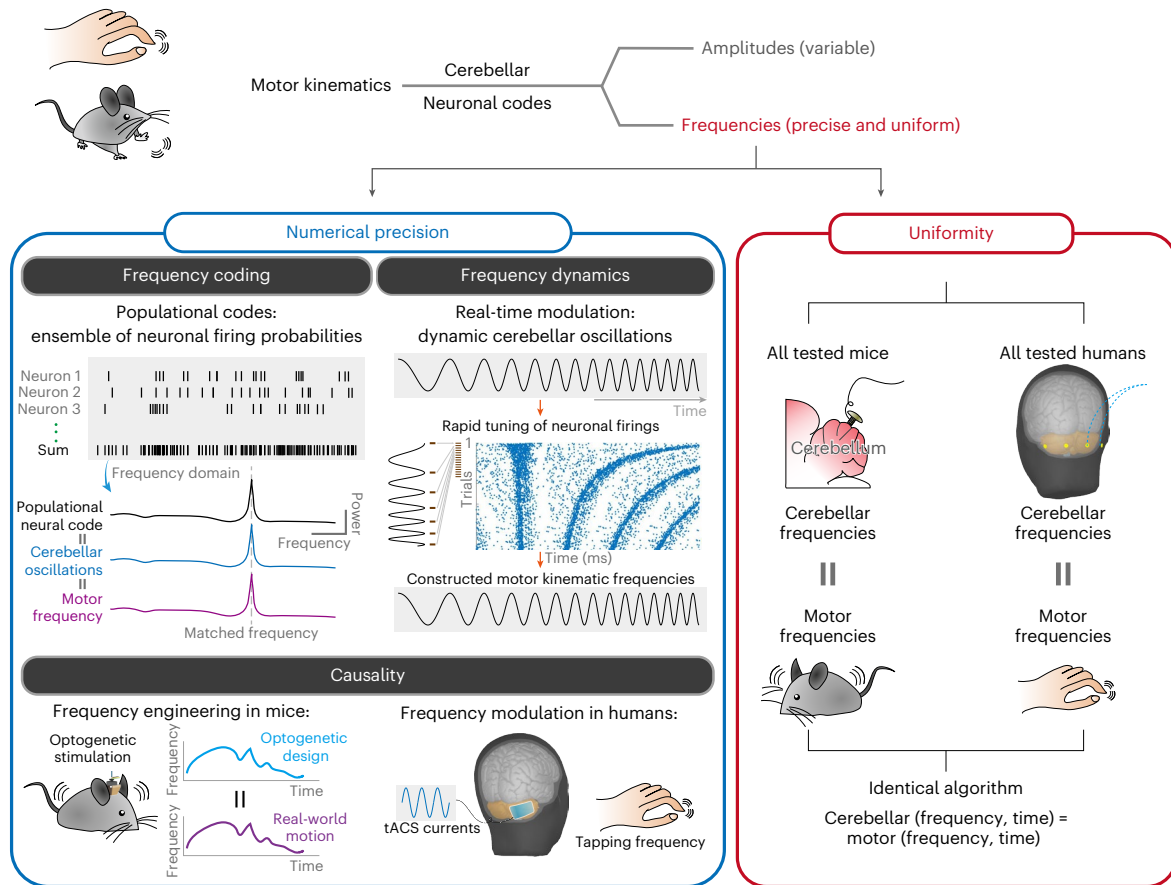


Fig. 8 | Summary of cerebellar frequency coding for motor kinematics. The cerebellum encodes dynamic motor frequencies for kinematics, with supreme numerical precision and cross-individual consistency. The motor frequencies are generated by integrating neuronal firing probabilities at the populational level. The motor frequencies can be highly dynamic across time

to construct non-rhythmic movements. The causality of the frequency-coding mechanism can be established by optogenetic manipulation in mice and current stimulations in humans. The cerebellar frequency codes for motion in both mice and humans are identical.

platform for physiological global movements with multiple muscle groups activated at the same frequency. This approach enhanced the frequency-related information against the background, but lost the topographical information of muscle groups. The skilled licking movements only involved tongue muscles and minimized topographical concerns. Future studies are required to demonstrate topography-based frequency coding for detailed motor kinematics. Second, we presented the human evidence that supports the causative roles of frequency modulation of the cerebellum by tACS interventions. However, we did not have the single-cell level of evidence to describe whether mouse and human cerebellar oscillations are generated based on the same mechanism of populational neuronal codes. Addressing this gap will probably require intrasurgical recordings or other methods capable of capturing detailed neuronal activity. There is also a limitation in the tACS experiment. The frequency-dependent phase relationship between cerebellar oscillations and stimulating currents remains unknown. Since the stimulation frequency matches the cerebellar LFP frequency, the stimulation artefacts prevented us from directly measuring this relationship using EEG. The tACS experiment provided evidence that cerebellar oscillations at the stimulation frequency can modulate human volitional movements at the targeted frequency, which is our goal in this experiment. Gathering further evidence would require more sophisticated approaches in future studies by indirectly monitoring the phase relationship between cerebellar oscillations and the stimulation.

The cerebellum employs a simple yet mathematically precise algorithm to manage the complexity and diversity of motor functions,

offering a potential biological strategy to address the known problem of ‘combinatorial explosion’ associated with nearly infinite motor patterns. This finding has several important implications for bioengineering. First, the frequencies of cerebellar signals are quantifiable and can be mathematically described, presenting an opportunity to create programmable control systems for biological movements using brain-computer interfaces (BCIs). Second, this frequency coding is achieved through population coding, which can be detected using techniques such as LFP or EEG. This opens the door to using less-invasive BCIs, such as epidural high-density arrays, for topography-specific frequency detection. A major advantage of this approach is to avoid invasive electrode arrays that penetrate the brain to record SU activity, which can lead to long-term neuronal damage and signal loss due to gliosis. Additionally, optogenetic manipulation of neuronal populations enables frequency-specific control of movement without the need for single-neuron resolution. Currently, experimental BCIs targeting the primary motor cortex still require invasive SU recordings for precise motor decoding, and the reliance on single-neuron microstimulation limits the kinematic precision achievable with simulation-based motor control. In contrast, cerebellar mechanisms may offer a less-invasive alternative. Third, and arguably the most important engineering implication, is that cerebellar frequency codes exhibit consistency across different individuals, both in mice and humans. This cross-individual consistency simplifies BCI design compared with purely customized BCIs that rely on model-free deep learning, as seen in the primary motor cortex. The consistency of these frequency codes in kinematic control provides valuable domain knowledge, reducing the data load

and complexity needed for training BCIs. Additionally, this domain knowledge offers the potential to develop BCIs for patients already with brain injuries, who are unable to provide the optimal training data during their healthy states. A potential application of cerebellar BCI is in patients with cerebellar ataxia. Cerebellar ataxia, with a core symptom of involuntary arrhythmic movements, is due to various genetic and non-genetic causes of cerebellar degeneration and PC loss. Currently, most forms of cerebellar ataxia lack effective treatment. By elucidating the mechanism of frequency coding in the cerebellum, cerebellar BCI may facilitate the populational DCN neurons or remaining PCs to generate the necessary frequencies²⁸ at the appropriate time and in the correct topographical location. Further investigation is required to validate whether this approach can improve ataxic symptoms.

The population-coding mechanism depends on an anatomical feature of axonal convergence within the motor cascade. Ultimately, the population-encoded frequencies must converge onto a select few spinal motor neurons responsible for executing motor commands. Supporting this prediction, there are approximately 262,000 DCN neurons in monkeys²⁹, while there are only about 600 skeletal muscles that can differentiate among various motor frequencies, resulting in an approximate 500:1 ratio. Additionally, the convergence rate from PCs to DCN neurons is roughly 40:1 (ref. 30). This suggests that the cerebellar system exploits population convergence and redundancy to compute motor frequencies efficiently.

While the cerebellum nicely encodes motor frequency, there are frequency harmonics in neuronal and behavioural levels in both mice and human experiments. The deviation of waveforms from a pure sinusoidal shape is reflected in the presence of harmonics. Several mechanisms within the optogenetic-to-motor axis are known to generate these harmonics. First, the relationship between light intensity and photocurrents is sigmoidal, and the positive feedback mechanism in action potential generation is highly nonlinear. As a result, even when optogenetic stimulation is sinusoidal (for example, Fig. 6b,k), the probability of neuronal activation via optogenetics remains nonlinear, as demonstrated in Fig. 6h,p. The summation of this neuronal activity across a population may produce non-sinusoidal contributions to LFPs (Fig. 6b,k), which directly lead to harmonics from the neuronal building blocks. Second, additional nonlinear transformations may occur between neuronal activation and motor outputs. The cerebello-thalamo-cortical-spinal-muscular pathway introduces multiple nonlinear events, including synaptic transmission and action potential generation. This is illustrated in the human data (Fig. 7c), where volitional rhythmic tapping, driven by rhythmic cerebellar oscillations with minimal harmonics, results in brisk, non-sinusoidal EMG activation with pronounced harmonics.

Constructing motor kinematics requires information on both motor frequencies and amplitudes. While the cerebellum can precisely construct dynamic motor frequencies, the counterpart mechanism for motor amplitude coding remains elusive and more complex. Our current findings (Figs. 2 and 4–7) and previous studies^{15,16,31} in both mice and humans suggested that the cerebellum can also regulate motor amplitudes. Yet variations in motor amplitudes under consistent levels of optogenetic stimulation or cerebellar oscillations indicate the presence of additional mechanisms beyond cerebellar oscillations and population coding. Future research needs to elucidate the mechanisms responsible for encoding instantaneous amplitudes, which are crucial for constructing functional motor kinematics.

This work did not investigate the neuronal activities in the inferior olive, which is the primary source of climbing fibres that project to the cerebellar cortex in a highly organized and modular pattern^{32–36} and plays an essential role in timing, rhythm, amplitude control of movement^{8,11,12,37–42} and motor learning^{4,43–57}. While our work emphasizes the precise population-level frequency coding in the DCN and the engineerable aspects of motor control, it is essential to acknowledge the foundational studies and theories that have shaped our

understanding of olivocerebellar motor control. The cerebellar cortex is organized into longitudinal strips^{36,58}, where PCs within each strip receive climbing fibre inputs with similar receptive fields, forming functional units known as microzones^{59–69}. These microzones are connected to specific regions of the inferior olive and project to the same cerebellar nuclei. This unique structural organization allows parallel information processing and plays a critical role in sensorimotor control^{61,63,66,69} and coordination of multijoint movements^{70,71}. Stimulation of different regions within the cerebellar nuclei, corresponding to different microzones, has been shown to evoke multijoint muscle movements across different limbs^{27,71}. Our findings align with this foundational understanding by demonstrating that optogenetics stimulation of the DCN can elicit rhythmic movements in the right forelimb (Supplementary Fig. 14 and Supplementary Video 4). Beyond its structural connectivity, the cerebellum has been proposed as a computational model for supervised learning and pattern recognition, utilizing climbing fibres to provide error signals that guide synaptic plasticity at parallel fibre–PC synapses^{51–57}. This framework supports the cerebellum's role in motor control through internal models^{54,72,73} that enable learning, adaptation and error correction. While some argue that cerebellar kinematic control is a secondary effect solely derived from motor learning, our study provides direct evidence of real-time kinematic control. Specifically, the optogenetically induced movements evoked by complex chirps are precise from the very first instance, with no time or consistent patterns available for the mice to learn. The cerebellar mechanisms of time keeping, motor learning, motor control and sensory feedback are not mutually exclusive but rather operate collaboratively to shape precise motor kinematics. This study leverages advances in population microelectrode recordings, which not only support previous findings on single-neuronal temporal coding of movement, but also extend the evidence to unprecedented precision and cross-individual uniformity through the mechanism of population coding. While alternative theories attribute different roles to the olivocerebellar system in motor control, which do not depend on subthreshold oscillations^{4,15,27,32–36,43–73}, our study focused on the downstream outcome of cerebellar computations in final motor output. The applicability of our findings under these alternative theories has not been examined in this work. Future studies are required to understand how the olivocerebellum interacts with the DCN populational codes for motor frequency control.

Methods

Animals

All experimental procedures were conducted following the guidelines and approved by the Institutional Animal Care and Use Committee of National Taiwan University (protocol numbers B201900034, B202000003 and B202100150). Mice were housed in the central and satellite facilities of National Taiwan University with a reversed 12 h light/12 h dark cycle and unrestricted access to water and food. Temperature and humidity were controlled within 22 ± 3 °C and $55 \pm 10\%$, respectively. All experimental mice were between 3 months and 1 year of age. C57B6/JNarl were used as WT mice. For optogenetic stimulation in the DCN, we used *Thy1-ChR2-EYFP* mice (B6.Cg-Tg(Thy1-COP4/EYFP)9Gfng/J, Jackson Laboratory, number 007615), which express ChR2-EYFP in various brain regions including our target DCN. For optogenetic stimulation in the PCs, we crossed *Calbindin-Cre* mice (B6;129S-*Calb1*^{tm2.1(cre)Hze}/J, Jackson Laboratory, number 028532) with Ai32 mice (B6;129S-*Gt(ROSA)26Sor*^{tm32(CAG-COP4*H134R/EYFP)Hze}/J, Jackson Laboratory, number 012569). The resulting calbindin × Ai32 mice express channelrhodopsin-2 dominantly in PCs.

Motion recordings in freely moving mice

Motion signals of mice were amplified and detected using a 15 × 22 cm force-sensitive platform (Convuls-1, Columbus Instruments; or custom¹⁶), allowing the mice to move freely. The platform linearly

converted the applied weight into voltage for recording, with a conversion rate of 0.45 volts per Newton (or 141 millivolts per 32 grams of mass per gravity), enabling the platform to sense subtle weight changes caused by the mice's motion. The data were then low-pass filtered at 250 Hz and then digitized at 1,000 Hz using a data acquisition (DAQ) device (Cerebus, BlackRock microsystem). Detailed information regarding the systems and settings can be found in our previous paper¹⁵.

Optetrode implantation and electrophysiology recording

Optetrode⁷⁴, a combination of tetrode and optical fibre, was applied to record SU activity, deep LFPs and perform optogenetic manipulation simultaneously. The construction of the optetrode involved threading tungsten tetrodes (California Fine Wire Company) and an optical fibre (ThorLabs, FT200UMT) through a microdrive screw (Renishaw) in a 3D-printed tower to stabilize and secure them. Each individual tungsten wire of the tetrode was threaded through the channel holes of the electrode interface board and anchored using gold pins. Additionally, we utilized small screws (Antrin Miniature Specialties, 0.089 inches in diameter, 0.0625 inches in length) as electrodes to record the LFPs of brain surface of mice.

During the surgery, 3-month-old mice were fixed on the stereotaxic frame under anaesthesia with isoflurane. The optetrodes were implanted at the DCN (anteroposterior (AP), -6.24 mm; mediolateral (ML), ± 2.1 mm; dorsoventral (DV), -1.9 mm from dura), and the screws were implanted on bilateral cerebellum surface (AP, -6.24 mm; ML, ± 2.1 mm). For hippocampal recordings, optetrodes were implanted at AP -2.65 mm, ML -3.0 mm and DV -2.0 mm from the dura. To identify the implanted trajectory of the optetrode, NeuroTrace Dil (Thermo Fisher, N-22800), a tissue-labelling paste, was applied to coat the surface of the optetrode. After the implantation, we applied dental cements (Superbond, Sun Medical) on the skull to secure the electrodes in place at the end of the surgery.

Electrophysiology signals were sampled at a rate of 30,000 Hz using a DAQ device (Cerebus, BlackRock microsystem or Open Ephys) for subsequent offline analysis, which will be described in detail in the following sections.

Optogenetic stimulation in the cerebellum

We utilized a custom-written LabView code to trigger the output of a diode laser (Cobolt, 473 nm) through a multifunction input/output device (NI 782258-01). This set up allowed us to precisely and linearly tune the output power at a frequency of 2 MHz. The laser power was adjusted individually for each mouse and ranged from 0.5 mW to 5 mW, to achieve observable rhythmic movement with a motion amplitude of approximately 10 millivolts on the force plate (corresponding to a conversion rate of 0.45 volts per Newton; see 'Optetrode implantation and electrophysiology recording' section). To ensure accurate light power levels, daily calibrations were performed using power meters (Thorlabs) before the experiments.

Most experiments involved optogenetic stimulation in Thy1-ChR2-EYFP mice. For enhanced specificity in DCN-dependent frequency coding, we also conducted experiments in WT mice injected with AAV9-hSyn-ChR2-EYFP (Addgene). In these cases, we performed unilateral injections into the DCN (AP, -6.24 mm; ML, 2.1 mm; DV, -2.0 mm from dura; 1 μ l). Optetrodes were then implanted in the target areas. The behavioural experiments started 3 weeks after the surgery for virus transfection.

In the experiments using multiple stimulating frequencies, trains of blue light (25% duty cycle) at 8, 12, 16, 20, 15 and 10 Hz were sequentially given for 90 s, separated by 300 s light-off periods. In the chirp stimulation experiment, linear chirp waves (30 s, from 4 Hz to 25 Hz) and complex chirp waves (1–10 s: 4–14 Hz; 10–15 s: 14–8 Hz; 15–25 s: 8–25 Hz; 25–30 s: 25–20 Hz; 30–35 s: 20 Hz; 35–45 s: 20–10 Hz; 45–50 s: 10 Hz; 50–60 s: 10–4 Hz) were generated by the MATLAB function and linearly transformed into laser power with the 30,000 Hz amplitude

updating rate. In experiments of varying laser intensities, trains of blue light (25% duty cycle) were delivered to the right DCN at a constant frequency of 16 Hz, with amplitudes incrementally increased from 0.5, 1, 2, 4 to 8 mW. All mice that received optogenetic stimulation were not exposed to the vibration platform before the stimulation experiments.

Vibration platform

We applied a customized vibration platform with optical grating to ensure precise control of vibration frequency and its sinusoidal vibrating waveform up to 120 Hz at the amplitude of 3 mm horizontal vibrations. Two cameras were set to capture the front view and top view of the vibration platform. In the experiments using multiple vibrated frequencies, the platform vibrated at 8, 12, 16, 20, 15 and 10 Hz sequentially, with a duration of 90 s in each frequency and separated by 2 min of non-vibrating periods. In the chirp vibrated experiment, 10 chirp vibration periods (30 s, from 4 Hz to 25 Hz) were separated by 30 s of non-vibrating periods, and we repeated the protocol for 10 times in each experimental section. In the dual-vibration frequencies experiment, we employed 3 sections of sinusoidal vibration signals at frequencies of 13 Hz and 20 Hz, and a combined signal at 13 Hz and 20 Hz. The combined signal was generated by summing sinusoidal signals at 13 Hz and 20 Hz. Each vibrating section lasted for 90 s, followed by a 120 s non-vibrating interval. We used the Open Ephys acquisition board to record neural electrophysiology signals, mouse accelerating signals and vibrated signals. Mouse accelerating and vibrated signals were captured through a headstage containing an accelerometer and an accelerometer attached to the vibration platform, respectively. The signals were recorded and digitized at the sampling rate of 30,000 Hz. To obtain the compensated motion signals, we applied a band-pass filter within the frequency range of 3–30 Hz to the vibrated signals and the mouse accelerating signals. We subtracted the mouse accelerating signals from the vibrated signals, resulting in the compensated motion signals.

In the vibration platform experiment, mice typically took 3–7 days to adapt. Each day, the mice underwent five vibration sessions with settings identical to those used in the actual experiments. Initially, owing to the freely moving set up, untrained mice would grip the platform's edge firmly and remain stationary. During early trials, the mice often slipped on the platform and quickly moved to the edge, where they would hold on and lean against the wall. Mice were considered well trained when they could move, explore and hop freely on the platform without slipping or edge gripping. Experiments and electrophysiological recordings were conducted only after the mice had achieved this level of training.

SU spike sorting and burst detection

Spikes were sorted by either of two sorting tools, Offline Sorter (OFS) software and Kilosort3 software⁷⁵. Electrophysiology data acquired through optetrode were high-pass filtered at 250 Hz, and the noise was reduced through digital referencing. Offline Sorter focuses on those with higher amplitude, and extracts them as spikes. Subsequently, it performs *K*-means clustering to assign each extracted spike to specific SUs. Kilosort3 models the electrophysiology data as a sum of template waveforms triggered on the spike times, enabling the identification and resolution of overlapping spikes. The detection criteria of DCN bursts followed previous studies^{17,76,77}. The interspike interval within a burst should be equal to or smaller than 15 ms. The minimal spike count within a burst was 4.

Spectrum analysis of motion and LFP data

The LFP data underwent spectrum analysis following the procedures consistent with our previous works^{15,17,78,79}. In summary, we placed the recording electrodes on bilateral cerebellar surface with the following coordinates relative to bregma: AP, -6.24 mm; ML, ± 2.1 mm; DV -0.1 mm (indentation without punch through dura). The reference

and ground electrodes were fixed into the right and left nasal bone, respectively. Signals from the two electrodes were subtracted from each other to form a typical bilateral montage with emphasis on the in-between signals in the motor cerebellum. The digitized data were originally sampled at 30,000 Hz and downsampled to 1,000 Hz for analysis with a band-pass filter set between 0.3 and 128 Hz. Frequency domain analysis was performed using in-house MATLAB scripts, with the following details. Welch's method with a Hanning window (each segment is 1 s long and overlaps half of the samples) was utilized to estimate power spectral density (PSD, $\mu\text{V}^2 \text{Hz}^{-1}$ for LFP data and $\text{mV}^2 \text{Hz}^{-1}$ for motion data). For fixed frequency stimulation, each PSD data point was calculated from a 20 s window with a 1 s shift. For chirp-wave stimulation, a 1 s window without overlap was applied.

EMG implant and analysis

In a subset of mice, we also implanted annealed wires (A-M system, 793500) into quadriceps muscles for EMG recording. The wires were tunnelled within the subdermal space and connected into the connector of a head-mounted connector. We followed the same DAQ settings for cerebellar LFP recordings. The EMG signals were preprocessed with a typical band-pass filter at 20–500 Hz for EMG.

Motion capture

To demonstrate the laterality of ipsilateral control in limb movements, each mouse was head fixed during optogenetic stimulation, and limb movements were recorded with a high-speed camera at 120 frames per second. Using DeepLabCut⁸⁰, a markerless pose estimation tool based on deep neural networks, we tracked the positions of both front paws. For subsequent spectrum analysis, we focused on the *x*-axis positions, as the primary movements occurred along this horizontal axis.

Vector strength analysis

The analysis of SU spike timing modulation was carried out using vector strength analysis. It was introduced by Goldberg and Brown in 1969 and has been widely utilized to quantify the phase locking and synchronization of a spike train, indicating whether a SU fires at specific phases of a particular modulation frequency^{20–24}. The spike timings of individual units were obtained using the methods discussed earlier, and these spike times, represented as a vector (**t**), were converted into phase angles (**p**) using the formula

$$\mathbf{p} = 2\pi f \mathbf{t},$$

where *f* represents frequency. Phase angles were adjusted to range from $-\pi$ to π . The vector strength (**v**) is then calculated with the equation below⁸¹ as

$$\mathbf{v} = \frac{1}{n} \left| \sum_{j=1}^n e^{i\mathbf{p}_j} \right|,$$

where *n* is the count of spikes, **p** is the vector of phase angles, *i* is the imaginary unit and *e* is Euler's number. Since a higher number of spikes often leads to a smaller vector strength, we normalized the vector strength to account for this bias⁸². We first generated a distribution of random vector strengths for *n* number of spikes by calculating vector strength with *n* random phases in 20,000 iterations. The mean and standard deviation of this distribution are then calculated, and the normalized vector strength is the original vector strength subtracting the mean and dividing the standard deviation.

The above steps only result in the vector strength at a certain frequency. To obtain a vector strength spectrum illustrating the frequencies at which the spike train achieves phase locking, the aforementioned steps were repeated for each frequency ranging from 1 Hz to 50 Hz with a 0.01 Hz increase. The resulting spectrum was then subjected to the removal of exponential decay and smoothed using a

Gaussian-weighted moving average. Prominent peaks with prominence larger than 1% of the mean intensity in the smoothed spectrum were subsequently identified. The prominence criteria prevent reporting random fluctuations, and the definition of prominence is defined in the MathWorks documentation page (<https://www.mathworks.com/help/signal/ref/findpeaks.html>). By iterating the steps above ten times with shuffled spike times and averaging them, we acquired the shuffled vector strength that served as a control.

To assess the contribution of population coding, we summed the normalized vector strength spectra from individual units in a random sequence one by one. This resulted in a cumulative spectrum and we examined the SNR from the inclusion of 10%, 20%, 40% and 80% of the total units. The SNR is defined as

$$\text{SNR} = \frac{\text{mean}(\text{signal})^2}{\text{s.d.}(\text{noise})^2},$$

The range of 'noise' pertains to a bandwidth of 5 Hz characterized by the least intensity. To mitigate potential bias, this iterative procedure was replicated 100 times. All these procedures were executed using an in-house MATLAB script.

Correlation spectrum (autocorrelogram)

We conducted an analysis of the firing modulation of SUs to assess their periodic activity. The SU data was downsampled from 30,000 Hz to 250 Hz and subsequently binarized into an array containing either 0 (indicating time without spike firing) or 1 (indicating time with spike firing). This binary array underwent autocorrelation using a maximum lag of 1 s, resulting in an autocorrelation function. To determine the firing modulation of the SU, we applied the fast Fourier transform (FFT) to the autocorrelation function with a frequency resolution of 0.1 Hz. We extracted prominent frequency components by identifying peaks in the frequency spectrum of the firing modulation, with a prominence exceeding 1% of the mean intensity. As with our vector strength analysis, our examination focused on the frequency range of 0–30 Hz, which corresponds to linear motor kinematic coding. We replicated the approach of unit summation as the vector strength spectrum. The definition of the SNR remained consistent. All the procedures detailed above were implemented using an in-house MATLAB script.

Spike-phase analysis

To examine the phasic tuning relationship between the SU-firing probability and the continuous data (cerebellar LFP and the motor kinematics), we coupled the SU spikes time with the instantaneous phase of the continuous data. First, both the SU spikes time and the LFP were downsampled from 30,000 Hz to 1,000 Hz to facilitate effective filtering. Next, we applied a band-pass filter to the continuous data with a range of ± 3 Hz around the frequency of interest (for example, 4, 8, 12, 16, 20, 15 and 10 Hz). Utilizing the Hilbert transform, we calculated the instantaneous phase of the filtered data and corrected it by $\pi/2$. Extracting the phase corresponding to each SU spike time, we visualized these extracted phases as polar histograms. Furthermore, we introduced a control by shuffling the instantaneous phases and pairing these randomized phases with each spike time, resulting in shuffled polar histograms. To quantify the phasic bias, we computed the polarity index¹⁵. This index involves summing each phase as a unit vector and then dividing by the total number of vectors. The polarity index ranges between 0 (indicating a purely random distribution across phases) to 1 (indicating a completely biased distribution towards a specific phase).

Correlation analysis of cerebellar LFP data

To examine the relationship between cerebellar LFP and various signals (vibrated signals, accelerating signals, motion signals and chirp stimulation signals of laser), we calculated their cross-correlation using an in-house MATLAB script based on the `xcorr()` function.

The cross-correlation was computed with a 1 s window that shifted along the data. As cross-correlation is a function of time shifts, we extracted the maximal value from each calculation across the shifting time.

Two-dimensional correlation analysis of chirp stimulation pattern

An ideal stimulation pattern generated from the chirp wave mentioned previously was obtained by aligning each stimulation point at 0 and plotting all stimulation points from -50 ms to 200 ms. The evoked spike times of DCN SUs were aligned and plotted in the same way, resulting in two-dimensional (2D) binary matrices of the same dimension. The 2D correlation coefficient between the ideal stimulation pattern and the experimental results was calculated, producing a single value indicating the similarity between the patterns. Shuffled patterns were generated by permutating the time points of DCN SU spikes. All the steps mentioned above were achieved by in-house MATLAB script.

Computational simulation

The neuron model. We used the leaky integrate-and-fire model as described previously^{83–85}. In the model, the membrane potential V of a neuron is given by

$$C \frac{dV}{dt} = -g_L(V - V_L) - g_s s(V - V_s) + I,$$

where C is the membrane capacitance, g_L is the membrane leak conductance, V_L is the membrane resting potential, g_s is the synaptic conductance, s is the synaptic gating variable, V_s is the synaptic reverse potential and I is other input currents. We further simplified the model into the following equivalent form by dividing both sides by C , which leads to

$$\frac{dV}{dt} = -\frac{1}{\tau}((V - V_L) + g'_s s(V - V_s) - i).$$

The conductance on the right-hand side of the equation is absorbed into $1/C$. As a result, g'_s is a unitless variable, and the input i has the unit of voltage. In the model, we also added Gaussian noise as the membrane current, which is given by $\sqrt{\tau}\sigma\chi$, where χ is a Gaussian distributed noise with zero mean and the unit s.d., and σ describes the magnitude of the noise. Adding the noise term into the equation above leads to

$$\frac{dV}{dt} = -\frac{1}{\tau}((V - V_L) + g'_s s(V - V_s) - i) + \frac{\sigma\chi}{\sqrt{\tau}}.$$

The gating variable s is given by

$$\frac{ds}{dt} = -\frac{s}{\tau_s} + \sum_k \delta(t - t_k),$$

where τ_s is the synaptic time constant and t_k is the time of k th input spike. The delta function $\delta(x)$ is ∞ at $x=0$ and 0 elsewhere. We modelled the excitatory and inhibitory (GABAergic) synapses. The time constant (τ_s) equals 2 ms for both types of synapses, and the reverse potential (V_s) is 0 mV for the excitatory and -70 mV for the inhibitory synapses.

The network model. The network contains two neural populations, PC and DCN, and each population contains 100 neurons. Each PC neuron exhibits a spontaneous firing rate at around 100 Hz due to the Gaussian noise input. A sinusoidal input $i = A \sin(2\pi ft)$ with amplitude, $A = 80$ mV, and modulatory frequency, $f = 16$ Hz, is also provided to the PC neurons. The PC neurons project to the DCN neurons with one-to-one connections via GABAergic synapses ($g'_s = 0.7$). The DCN neurons are known to exhibit spontaneous activity, which is modelled by applying a constant membrane current ($i = 20$ μ A) and a Poisson

spike train (100 Hz) through the excitatory synapse ($g'_s = 0.3$) to each DCN neuron. These inputs elicit a spontaneous firing rate of about 20–22 Hz in each DCN neuron.

LFPs. The LFPs of DCN are derived by calculating the mean excitatory postsynaptic current (EPSC) and mean inhibitory postsynaptic current (IPSC) across all DCN neurons and then taking the average of the two mean currents. The EPSC contributes to the negative component of the LFP, while the IPSC contributes to the positive component of the LFPs⁸⁶. We did not consider the distance factor of the neuron in relation to its contribution to the LFPs because we only modelled 100 DCN neurons, and no topographical correlation between these neurons was assumed.

The simulation protocol. We performed a 20,000 ms simulation in each trial. The first 5,000 ms was the resting period in which no sinusoidal input to the PC neurons was provided. PC neurons generally fired at around 100 Hz owing to the Gaussian noise input. After resting, the trial entered a 10,000 ms stimulation period in which the sinusoidal input to the PC neurons was turned on. After the stimulation period, the sinusoidal input was removed, and the trial entered a 5,000 post-stimulation resting period. The spike times EPSC and IPSC of all DCN neurons were recorded during the trial.

Data analysis. We calculated the power spectrum density of LFP and analysed the vector strength of the spike trains of the DCN neurons using methods similar to those described in Methods section of the main text. The LFP spectrum was calculated using Welch's method with a Hanning window of 1 s. The vector strength was calculated for different numbers of included units (neurons) to reveal the effect of population coding. The vector strength was normalized by subtracting the mean and then divided by the standard deviation of the random baseline data, which was calculated based on the vector strengths of 1,000 randomized spike trains.

Tissue clearing and histological validation

After completing the behavioural experiments, mice were perfused transcardially with 4% paraformaldehyde. Their brains were retrieved for further examination of electrode placement and fluorescent expression. Coronal or sagittal sections of were cut with a thickness of 500 μ m using a vibratome, and underwent tissue clearing with RapidClear (Bio-East Technology) for 1 week. The histology images were acquired with a fluorescent confocal microscope (SP8, Leica). We assessed both the electrode placement and the fluorescent expression pattern of *Thy1-ChR2-EYFP* and calbindin \times Ai32. In cases where improper electrode placement or insufficient fluorescent expression was observed, the corresponding electrophysiology data from those mice were excluded from further analysis.

Human subjects

Ten healthy subjects received cerebellar EEG recordings during volitional tapping, and six healthy subjects received the tACS study. We recruited these subjects from two institutions: the Neurological Institute at Columbia University Irving Medical Center, New York, USA, and the Cerebellar Research Center at National Taiwan University Hospital, Yun-Lin Branch, Yun-Lin, Taiwan. Before participating in the study, all subjects provided written consent. The research protocols were approved by the institutional review boards at both Columbia University and National Taiwan University Hospital. Further detailed information about the demographic of the subjects can be found in Supplementary Table 1.

Cerebellar EEG recordings and analysis for healthy subjects performing volitional tapping

The cerebellar EEG recordings were also performed with the same lead settings as our previous works^{15,31,87}. In healthy subjects performing

volitional tapping, the EEG signals were sampled at 512 Hz with a 64-channel EEG machine (Quantum, Natus Medical). The signals also received band-passed filter at ~ 0.3 –128 Hz. Muscle activities were recorded by surface EMG, also sampling at 512 Hz by the same EEG machine and band-pass filtered between 20 and 128 Hz. Surface EMG data were then enveloped based on the 20-ms of root mean-squared value by an in-house MATLAB function. The preprocessed EEG and enveloped EMG data then underwent the same spectrum analysis described previously.

Accelerometer measurements and tACS

In tACS experiments, the acceleration of finger tapping and EEG were recorded using the Brain Vision acceleration sensor MR (3D) and the actiCHamp system (Brain Vision LLC). To perform tACS, we utilized a Soterix Medical 1×1 tES mini-CT device to generate a stimulated waveform, which was then delivered using two 5×5 cm SNAPpad sponges (Soterix Medical) consisting of a pre-inserted carbon-rubber electrode at an intensity of 2.5 mA. These sponge electrodes were firmly secured in place using a head and arm SNAPstrap. The stimulation electrode was targeted at 2 cm lateral to theinion, covering the right cerebellar hemisphere, while the reference electrode was positioned on the deltoid muscles of the right arm.

The experiment involved a sound-guided, rhythmic tapping task using the index finger. Baseline recording involved 2 min of tapping, including 1 min of tapping with 4 Hz guided audio sound, and 1 min of tapping without any audio. After a short rest interval, tACS was delivered for 2 min during the tapping task at 4 Hz. The audio cue was applied for 1 min in every tapping period and then turned off. After stimulation and a rest interval, the tapping task was repeated and recorded again for 2 min, including 1 min of tapping with guided audio sound and 1 min without any audio.

To assess the phase stability between the accelerometer-recorded motion and tACS, we applied the phase-sensitive cross-correlation. We transformed the motion while preserving its frequency dynamics and eliminating amplitude fluctuations by extracting their Hilbert-based instantaneous phases and replacing with the time-dependent phases of a unit vector. The transformed motion was then cross-correlated with the 4 Hz sine waves, to evaluate the rhythmicity between 4 Hz tapping and perfect 4 Hz signals. The maximal cross-correlation values were calculated. To ensure fair comparisons among subjects, we normalized the mean cross-correlation values (averages of cross-correlation values across the entire experiment) to 1.

Statistics

Non-parametric analyses were conducted for datasets with sample sizes below 35 or those not following a normal distribution. We applied the Mann–Whitney *U* test, Wilcoxon signed-rank test and Kruskal–Wallis test for independent samples, paired groups and multiple groups, respectively. For datasets with sample sizes exceeding 35 and meeting the homogeneity test for normal distribution, Student's *t*-test, paired *t*-test and one-way analysis of variance (ANOVA) were employed for independent samples, paired samples and multiple groups, respectively. Raw data points are illustrated in the figures.

Reporting summary

Further information on research design is available in the Nature Portfolio Reporting Summary linked to this article.

Data availability

All data are available in the main text or Supplementary Information. Source data are provided with this paper.

Code availability

Programs for data analysis are available on Code Ocean at <https://doi.org/10.24433/CO.8551138.v2> (ref. 88). Further details are upon request.

References

- Biondi, A. et al. Are the brains of monozygotic twins similar? A three-dimensional MR study. *Am. J. Neuroradiol.* **19**, 1361–1367 (1998).
- Metzger, S. L. et al. A high-performance neuroprosthesis for speech decoding and avatar control. *Nature* **620**, 1037–1046 (2023).
- Becker, M. I. & Person, A. L. Cerebellar control of reach kinematics for endpoint precision. *Neuron* **103**, 335–348.e335 (2019).
- Calame, D. J., Becker, M. I. & Person, A. L. Cerebellar associative learning underlies skilled reach adaptation. *Nat. Neurosci.* **26**, 1068–1079 (2023).
- Wagner, M. J. et al. A neural circuit state change underlying skilled movements. *Cell* **184**, 3731–3747.e3721 (2021).
- Wagner, M. J. et al. Shared cortex–cerebellum dynamics in the execution and learning of a motor task. *Cell* **177**, 669–682.e624 (2019).
- Sedaghat-Nejad, E., Pi, J. S., Hage, P., Fakharian, M. A. & Shadmehr, R. Synchronous spiking of cerebellar Purkinje cells during control of movements. *Proc. Natl Acad. Sci. USA* **119**, e2118954119 (2022).
- Herzfeld, D. J., Kojima, Y., Soetedjo, R. & Shadmehr, R. Encoding of action by the Purkinje cells of the cerebellum. *Nature* **526**, 439–442 (2015).
- Llinás, R. & Wolfe, J. W. Functional linkage between the electrical activity in the vermal cerebellar cortex and saccadic eye movements. *Exp. Brain Res.* **29**, 1–14 (1977).
- Welsh, J. P., Lang, E. J., Suglhara, I. & Llinás, R. Dynamic organization of motor control within the olivocerebellar system. *Nature* **374**, 453–457 (1995).
- Llinás, R. & Volkind, R. A. The olivo-cerebellar system: functional properties as revealed by harmaline-induced tremor. *Exp. Brain Res.* **18**, 69–87 (1973).
- de Solages, C. et al. High-frequency organization and synchrony of activity in the Purkinje cell layer of the cerebellum. *Neuron* **58**, 775–788 (2008).
- Nguyen, T. M. et al. Structured cerebellar connectivity supports resilient pattern separation. *Nature* **613**, 543–549 (2023).
- Wang, X. et al. Excitatory nucleo-olivary pathway shapes cerebellar outputs for motor control. *Nat. Neurosci.* **26**, 1394–1406 (2023).
- Pan, M. K. et al. Cerebellar oscillations driven by synaptic pruning deficits of cerebellar climbing fibers contribute to tremor pathophysiology. *Sci. Transl. Med.* <https://doi.org/10.1126/scitranslmed.aay1769> (2020).
- Ni, C. L. et al. Tracking motion kinematics and tremor with intrinsic oscillatory property of instrumental mechanics. *Bioeng. Transl. Med.* **8**, e10432 (2022).
- Wang, Y. M. et al. Neuronal population activity in the olivocerebellum encodes the frequency of essential tremor in mice and patients. *Sci. Transl. Med.* <https://doi.org/10.1126/scitranslmed.adl1408> (2024).
- Kuo, S. H. et al. Climbing fiber–Purkinje cell synaptic pathology in tremor and cerebellar degenerative diseases. *Acta Neuropathol.* **133**, 121–138 (2017).
- Louis, E. D. et al. Histopathology of the cerebellar cortex in essential tremor and other neurodegenerative motor disorders: comparative analysis of 320 brains. *Acta Neuropathol.* **145**, 265–283 (2023).
- Goldberg, J. M. & Brown, P. B. Response of binaural neurons of dog superior olivary complex to dichotic tonal stimuli: some physiological mechanisms of sound localization. *J Neurophysiol.* **32**, 613–636 (1969).
- van Hemmen, J. L. Vector strength after Goldberg, Brown, and von Mises: biological and mathematical perspectives. *Biol. Cybern.* **107**, 385–396 (2013).

22. Heil, P. & Peterson, A. J. Basic response properties of auditory nerve fibers: a review. *Cell Tissue Res.* **361**, 129–158 (2015).
23. Heil, P. & Peterson, A. J. Spike timing in auditory-nerve fibers during spontaneous activity and phase locking. *Synapse* **71**, 5–36 (2017).
24. Kessler, D., Carr, C. E., Kretzberg, J. & Ashida, G. Theoretical relationship between two measures of spike synchrony: correlation index and vector strength. *Front. Neurosci.* **15**, 761826 (2021).
25. Dimitrova, A. et al. Activation of cerebellar nuclei comparing finger, foot and tongue movements as revealed by fMRI. *Brain Res. Bull.* **71**, 233–241 (2006).
26. Schreglmann, S. R. et al. Non-invasive suppression of essential tremor via phase-locked disruption of its temporal coherence. *Nat. Commun.* **12**, 363 (2021).
27. Rispal-Padel, L., Cicerata, F. & Pons, C. Cerebellar nuclear topography of simple and synergistic movements in the alert baboon (*Papio papio*). *Exp. Brain Res.* **47**, 365–380 (1982).
28. Lin, C. C. et al. Reduced cerebellar rhythm by climbing fiber denervation is linked to motor rhythm deficits in mice and ataxia severity in patients. *Sci. Transl. Med.* **17**, eadk3922 (2025).
29. Gould, B. B. & Rakic, P. The total number, time or origin and kinetics of proliferation of neurons comprising the deep cerebellar nuclei in the rhesus monkey. *Exp. Brain Res.* **44**, 195–206 (1981).
30. Xiao, L. & Scheiffele, P. Local and long-range circuit elements for cerebellar function. *Curr. Opin. Neurobiol.* **48**, 146–152 (2018).
31. Wong, S. B. et al. Cerebellar oscillations in familial and sporadic essential tremor. *Cerebellum* <https://doi.org/10.1007/s12311-021-01309-9> (2021).
32. Armstrong, D. M. Functional significance of connections of the inferior olive. *Physiol. Rev.* **54**, 358–417 (1974).
33. Apps, R. Columnar organisation of the inferior olive projection to the posterior lobe of the rat cerebellum. *J. Comp. Neurol.* **302**, 236–254 (1990).
34. Trott, J. R. & Apps, R. Lateral and medial sub-divisions within the olivocerebellar zones of the paravermal cortex in lobule Vb/c of the cat anterior lobe. *Exp. Brain Res.* **87**, 126–140 (1991).
35. Trott, J. R. & Apps, R. Zonal organization within the projection from the inferior olive to the rostral paramedian lobule of the cat cerebellum. *Eur. J. Neurosci.* **5**, 162–173 (1993).
36. Voogd, J. & Glickstein, M. The anatomy of the cerebellum. *Trends Neurosci.* **21**, 370–375 (1998).
37. de Montigny, C. & Lamarre, Y. Rhythmic activity induced by harmaline in the olivo-cerebello-bulbar system of the cat. *Brain Res.* **53**, 81–95 (1973).
38. Matsumoto-Makidono, Y. et al. Ionic basis for membrane potential resonance in neurons of the inferior olive. *Cell Rep.* **16**, 994–1004 (2016).
39. Lang, E. J., Sugihara, I. & Llinas, R. Olivocerebellar modulation of motor cortex ability to generate vibrissal movements in rat. *J. Physiol.* **571**, 101–120 (2006).
40. Lang, E. J., Sugihara, I. & Llinás, R. GABAergic modulation of complex spike activity by the cerebellar nucleoolivary pathway in rat. *J. Neurophysiol.* **76**, 255–275 (1996).
41. Handforth, A. & Lang, E. J. Increased Purkinje cell complex spike and deep cerebellar nucleus synchrony as a potential basis for syndromic essential tremor. A review and synthesis of the literature. *Cerebellum* **20**, 266–281 (2021).
42. Boven, E. & Cerminara, N. L. Cerebellar contributions across behavioural timescales: a review from the perspective of cerebro-cerebellar interactions. *Front. Syst. Neurosci.* **17**, 1211530 (2023).
43. Darmohray, D. M., Jacobs, J. R., Marques, H. G. & Carey, M. R. Spatial and temporal locomotor learning in mouse cerebellum. *Neuron* **102**, 217–231.e214 (2019).
44. Gutierrez-Castellanos, N. et al. Motor learning requires Purkinje cell synaptic potentiation through activation of AMPA-receptor subunit GluA3. *Neuron* **93**, 409–424 (2017).
45. Ohmae, S. & Medina, J. F. Climbing fibers encode a temporal-difference prediction error during cerebellar learning in mice. *Nat. Neurosci.* **18**, 1798–1803 (2015).
46. Yang, Y. & Lisberger, S. G. Purkinje-cell plasticity and cerebellar motor learning are graded by complex-spike duration. *Nature* **510**, 529–532 (2014).
47. Nguyen-Vu, T. D. et al. Cerebellar Purkinje cell activity drives motor learning. *Nat. Neurosci.* **16**, 1734–1736 (2013).
48. Morton, S. M. & Bastian, A. J. Cerebellar contributions to locomotor adaptations during splitbelt treadmill walking. *J. Neurosci.* **26**, 9107–9116 (2006).
49. Boyden, E. S., Katoh, A. & Raymond, J. L. Cerebellum-dependent learning: the role of multiple plasticity mechanisms. *Annu. Rev. Neurosci.* **27**, 581–609 (2004).
50. Braitenberg, V., Heck, D. & Sultan, F. The detection and generation of sequences as a key to cerebellar function: experiments and theory. *Behav. Brain Sci.* **20**, 229–245 (1997).
51. Ito, M. & Kano, M. Long-lasting depression of parallel fiber–Purkinje cell transmission induced by conjunctive stimulation of parallel fibers and climbing fibers in the cerebellar cortex. *Neurosci. Lett.* **33**, 253–258 (1982).
52. Albus, J. S. A theory of cerebellar function. *Math. Biosci.* **10**, 25–61 (1971).
53. Eccles, J. C. *The Cerebellum as a Neuronal Machine* (Springer, 2013).
54. Ito, M. Neurophysiological aspects of the cerebellar motor control system. *Int. J. Neurol.* **7**, 162–176 (1970).
55. Marr, D. A theory of cerebellar cortex. *J. Physiol.* **202**, 437–470 (1969).
56. Thach, W. T. Jr. Somatosensory receptive fields of single units in cat cerebellar cortex. *J. Neurophysiol.* **30**, 675–696 (1967).
57. Kawato, M., Ohmae, S., Hoang, H. & Sanger, T. 50 Years since the Marr, Ito, and Albus models of the cerebellum. *Neuroscience* **462**, 151–174 (2021).
58. Hawkes, R. Antigenic markers of cerebellar modules in the adult mouse. *Biochem. Soc. Trans.* **20**, 391–395 (1992).
59. Ekerot, C. F. & Larson, B. The dorsal spino-olivocerebellar system in the cat. II. Somatotopical organization. *Exp. Brain Res.* **36**, 219–232 (1979).
60. Ekerot, C. F. & Larson, B. Branching of olivary axons to innervate pairs of sagittal zones in the cerebellar anterior lobe of the cat. *Exp. Brain Res.* **48**, 185–198 (1982).
61. Garwicz, M. & Ekerot, C. F. Topographical organization of the cerebellar cortical projection to nucleus interpositus anterior in the cat. *J. Physiol.* **474**, 245–260 (1994).
62. Armstrong, D. M. Topographical localisation in the projections from the inferior olive to the paravermal cortex of the anterior lobe and paramedian lobule in the cerebellum of the cat. A brief review. *Arch. Ital. Biol.* **128**, 183–207 (1990).
63. Ito, M. The cerebellum: from structure to control. *Trends Cogn. Sci.* **2**, 371 (1998).
64. Oscarsson, O. Functional units of the cerebellum—sagittal zones and microzones. *Trends Neurosci.* **2**, 143–145 (1979).
65. Andersson, G. & Oscarsson, O. Climbing fiber microzones in cerebellar vermis and their projection to different groups of cells in the lateral vestibular nucleus. *Exp. Brain Res.* **32**, 565–579 (1978).
66. Hesslow, G. Correspondence between climbing fibre input and motor output in eyeblink-related areas in cat cerebellar cortex. *J. Physiol.* **476**, 229–244 (1994).
67. Garwicz, M., Apps, R. & Trott, J. R. Micro-organization of olivocerebellar and corticonuclear connections of the paravermal cerebellum in the cat. *Eur. J. Neurosci.* **8**, 2726–2738 (1996).

68. Apps, R. et al. Cerebellar modules and their role as operational cerebellar processing units. *Cerebellum* **17**, 654–682 (2018).
69. Apps, R. & Garwicz, M. Anatomical and physiological foundations of cerebellar information processing. *Nat. Rev. Neurosci.* **6**, 297–311 (2005).
70. Cooper, S. E., Martin, J. H. & Ghez, C. Effects of inactivation of the anterior interpositus nucleus on the kinematic and dynamic control of multijoint movement. *J. Neurophysiol.* **84**, 1988–2000 (2000).
71. Ekerot, C. F., Jörntell, H. & Garwicz, M. Functional relation between corticonuclear input and movements evoked on microstimulation in cerebellar nucleus interpositus anterior in the cat. *Exp. Brain Res.* **106**, 365–376 (1995).
72. Wolpert, D. M. & Kawato, M. Multiple paired forward and inverse models for motor control. *Neural Netw.* **11**, 1317–1329 (1998).
73. Wolpert, D. M., Miall, R. C. & Kawato, M. Internal models in the cerebellum. *Trends Cogn. Sci.* **2**, 338–347 (1998).
74. Anikeeva, P. et al. Optetrode: a multichannel readout for optogenetic control in freely moving mice. *Nat. Neurosci.* **15**, 163–170 (2011).
75. Pachitariu, M., Steinmetz, N., Kadir, S., Carandini, M. & Harris, K. Fast and accurate spike sorting of high-channel count probes with KiloSort. In *Proc. 30th International Conference on Neural Information Processing Systems* (eds Lee, D. D. et al.) 4455–4463 (Curran Associates, 2016).
76. Tadayonnejad, R. et al. Rebound discharge in deep cerebellar nuclear neurons in vitro. *Cerebellum* **9**, 352–374 (2010).
77. Molineux, M. L. et al. Specific T-type calcium channel isoforms are associated with distinct burst phenotypes in deep cerebellar nuclear neurons. *Proc. Natl Acad. Sci. USA* **103**, 5555–5560 (2006).
78. Pan, M. K. et al. Deranged NMDAergic cortico-subthalamic transmission underlies parkinsonian motor deficits. *J. Clin. Invest.* **124**, 4629–4641 (2014).
79. Pan, M. K. et al. Neuronal firing patterns outweigh circuitry oscillations in parkinsonian motor control. *J. Clin. Invest.* **126**, 4516–4526 (2016).
80. Mathis, A. et al. DeepLabCut: markerless pose estimation of user-defined body parts with deep learning. *Nat. Neurosci.* **21**, 1281–1289 (2018).
81. Lachaux, J. P., Rodriguez, E., Martinerie, J. & Varela, F. J. Measuring phase synchrony in brain signals. *Hum. Brain Mapp.* **8**, 194–208 (1999).
82. Herrmann, B., Parthasarathy, A. & Bartlett, E. L. Ageing affects dual encoding of periodicity and envelope shape in rat inferior colliculus neurons. *Eur. J. Neurosci.* **45**, 299–311 (2017).
83. Hsiao, P. Y. & Lo, C. C. A plastic corticostriatal circuit model of adaptation in perceptual decision making. *Front. Comput. Neurosci.* **7**, 178 (2013).
84. Lo, C. C., Boucher, L., Paré, M., Schall, J. D. & Wang, X. J. Proactive inhibitory control and attractor dynamics in countermanding action: a spiking neural circuit model. *J. Neurosci.* **29**, 9059–9071 (2009).
85. Lo, C. C. & Wang, X. J. Conflict resolution as near-threshold decision-making: a spiking neural circuit model with two-stage competition for antisaccadic task. *PLoS Comput. Biol.* **12**, e1005081 (2016).
86. Zheng, Y. et al. Balanced excitation and inhibition: model based analysis of local field potentials. *Neuroimage* **63**, 81–94 (2012).
87. Kumar, A., Lin, C. C., Kuo, S. H. & Pan, M. K. Physiological recordings of the cerebellum in movement disorders. *Cerebellum* **22**, 985–1001 (2023).
88. Liu, C. C. et al. The cerebellum shapes motions by encoding motor frequencies with precision and cross-individual uniformity. *Code Ocean* <https://doi.org/10.24433/CO.8551138.v2> (2025).

Acknowledgements

This research was supported by National Science and Technology Council (NSTC) in Taiwan (grant nos. 109-2326-B-002-013-MY4, 107-2321-B-002-020, 108-2321-B-002-011, 108-2321-002-059-MY2, 110-2321-B-002-012, 111-2628-B-002-036, 112-2628-B-002-011 and 113-2628-B-002-002 (to M.-K.P.)), National Taiwan University College of Medicine (grant no. NTUMC 110C101-011 (to M.-K.P.)), National Taiwan University Hospital (grant nos. NSC-145-11, 113-UN0013, 112-UN0024, 113-E0001 and 108-039 (to M.-K.P.)), Academia Sinica (grant no. AS-TM-112-01-02), National Health Research Institutes (grant nos. NHRI-EX113-11303NI and NHRI-EX114-11303NI (to M.-K.P.)) and the NIH (grant nos. R01NS118179, R01NS104423 and R01NS124854 (to S.-H.K.)). We thank The Featured Areas Research Center Program within the framework of the Higher Education Sprout Project co-funded by the NSTC and the Ministry of Education, Taiwan, the Excellent Translational Medicine Research Projects of National Taiwan University College of Medicine, and National Taiwan University Hospital for their support; and the technical assistance of the First Core Labs in the National Taiwan University College of Medicine. We thank Sun Medical Co. Ltd. for providing high-quality adhesives for surgical implants. We thank the participating subjects for human studies in National Taiwan University Hospital, Yun-Lin Branch.

Author contributions

M.-K.P. supervised the project, developed the theory and designed the experiments. Y.-M.W. and A.K. performed human electrophysiological studies in healthy subjects and tACS recordings. M.-K.P. and S.-H.K. supervised the tACS experiments. W.-C.L., P.C., T.-Y.L., K.-C.F., L.-Y.L., I.-C.L., C.-W.L. and S.-Y.C. performed electrophysiological recordings, optogenetics and behavioural recordings. S.-Y.C. and L.-Y.L. optimized the MATLAB codes for spike-sorting and signal-processing pipelines. J.-C.L. and W.-C.L. optimized the hardware of the vibration platform and coded the hardware-controlling interface. M.-K.P., C.-C.L. and W.-C.L. optimized the mathematical algorithms. All authors contribute to the writing of paper. M.-K.P. edited the paper.

Competing interests

The authors declare no competing interests.

Additional information

Supplementary information The online version contains supplementary material available at <https://doi.org/10.1038/s41551-025-01409-5>.

Correspondence and requests for materials should be addressed to Ming-Kai Pan.

Peer review information *Nature Biomedical Engineering* thanks Fredrik Bengtsson, Timothy Ebner and Dieter Jaeger for their contribution to the peer review of this work. Peer reviewer reports are available.

Reprints and permissions information is available at www.nature.com/reprints.

Publisher's note Springer Nature remains neutral with regard to jurisdictional claims in published maps and institutional affiliations.

Open Access This article is licensed under a Creative Commons Attribution-NonCommercial-NoDerivatives 4.0 International License, which permits any non-commercial use, sharing, distribution and reproduction in any medium or format, as long as you give appropriate credit to the original author(s) and the source, provide a link to the Creative Commons licence, and indicate if you modified the licensed material. You do not have permission under this licence to share

adapted material derived from this article or parts of it. The images or other third party material in this article are included in the article's Creative Commons licence, unless indicated otherwise in a credit line to the material. If material is not included in the article's Creative Commons licence and your intended use is not permitted by statutory

regulation or exceeds the permitted use, you will need to obtain permission directly from the copyright holder. To view a copy of this licence, visit <http://creativecommons.org/licenses/by-nc-nd/4.0/>.

© The Author(s) 2025

¹Department and Graduate Institute of Pharmacology, National Taiwan University College of Medicine, Taipei, Taiwan. ²Molecular Imaging Center, National Taiwan University, Taipei, Taiwan. ³Cerebellar Research Center, National Taiwan University Hospital, Yun-Lin Branch, Yun-Lin, Taiwan. ⁴Institute of Biomedical Sciences, Academia Sinica, Taipei, Taiwan. ⁵Department of Medical Research, National Taiwan University Hospital, Taipei, Taiwan. ⁶The Initiative for Columbia Ataxia and Tremor, New York, NY, USA. ⁷Department of Neurology, Columbia University, New York, NY, USA. ⁸Institute of Systems Neuroscience, National Tsing Hua University, Hsinchu, Taiwan. ⁹Department of Engineering and Bioinformatics, National Tsing Hua University, Hsinchu, Taiwan. ¹⁰These authors contributed equally: Chia-Wei Liu, Yi-Mei Wang, Shun-Ying Chen, Liang-Yin Lu. ✉e-mail: emorymkpan@ntu.edu.tw

Reporting Summary

Nature Portfolio wishes to improve the reproducibility of the work that we publish. This form provides structure for consistency and transparency in reporting. For further information on Nature Portfolio policies, see our [Editorial Policies](#) and the [Editorial Policy Checklist](#).

Statistics

For all statistical analyses, confirm that the following items are present in the figure legend, table legend, main text, or Methods section.

- | n/a | Confirmed |
|-------------------------------------|--|
| <input type="checkbox"/> | <input checked="" type="checkbox"/> The exact sample size (n) for each experimental group/condition, given as a discrete number and unit of measurement |
| <input type="checkbox"/> | <input checked="" type="checkbox"/> A statement on whether measurements were taken from distinct samples or whether the same sample was measured repeatedly |
| <input type="checkbox"/> | <input checked="" type="checkbox"/> The statistical test(s) used AND whether they are one- or two-sided
<i>Only common tests should be described solely by name; describe more complex techniques in the Methods section.</i> |
| <input checked="" type="checkbox"/> | <input type="checkbox"/> A description of all covariates tested |
| <input type="checkbox"/> | <input checked="" type="checkbox"/> A description of any assumptions or corrections, such as tests of normality and adjustment for multiple comparisons |
| <input type="checkbox"/> | <input checked="" type="checkbox"/> A full description of the statistical parameters including central tendency (e.g. means) or other basic estimates (e.g. regression coefficient) AND variation (e.g. standard deviation) or associated estimates of uncertainty (e.g. confidence intervals) |
| <input type="checkbox"/> | <input checked="" type="checkbox"/> For null hypothesis testing, the test statistic (e.g. F , t , r) with confidence intervals, effect sizes, degrees of freedom and P value noted
<i>Give P values as exact values whenever suitable.</i> |
| <input checked="" type="checkbox"/> | <input type="checkbox"/> For Bayesian analysis, information on the choice of priors and Markov chain Monte Carlo settings |
| <input checked="" type="checkbox"/> | <input type="checkbox"/> For hierarchical and complex designs, identification of the appropriate level for tests and full reporting of outcomes |
| <input type="checkbox"/> | <input checked="" type="checkbox"/> Estimates of effect sizes (e.g. Cohen's d , Pearson's r), indicating how they were calculated |

Our web collection on [statistics for biologists](#) contains articles on many of the points above.

Software and code

Policy information about [availability of computer code](#)

Data collection All electrophysiological data are collected by the Cerebus system (BlackRock microsystem, USA) with the Central Software (version 6.5.4)

Data analysis Statistics are performed with Prism (version 8.0.1) or Microsoft Excel (version 2019).
Spike sorting is performed with Kilosort 3.
The Matlab codes (version 2018b) used for this manuscript are available at Code Ocean:
<https://doi.org/10.24433/CO.8551138.v2>

For manuscripts utilizing custom algorithms or software that are central to the research but not yet described in published literature, software must be made available to editors and reviewers. We strongly encourage code deposition in a community repository (e.g. GitHub). See the Nature Portfolio [guidelines for submitting code & software](#) for further information.

Data

Policy information about [availability of data](#)

All manuscripts must include a [data availability statement](#). This statement should provide the following information, where applicable:

- Accession codes, unique identifiers, or web links for publicly available datasets
- A description of any restrictions on data availability
- For clinical datasets or third party data, please ensure that the statement adheres to our [policy](#)

Data and materials availability: All data are available in the main text or the supplementary materials. Programs for data analysis are deposited in Code Ocean

repository:
<https://doi.org/10.24433/CO.8551138.v2>
 Further details are upon request.

Research involving human participants, their data, or biological material

Policy information about studies with [human participants or human data](#). See also policy information about [sex, gender \(identity/presentation\), and sexual orientation](#) and [race, ethnicity and racism](#).

Reporting on sex and gender	Gender information is collected by informed consent and self-reporting. The information is provided in Table S1.
Reporting on race, ethnicity, or other socially relevant groupings	Race, ethnicity or social constructed is not grouped in this study.
Population characteristics	Age and gender are provided in Table S1. The subjects are healthy volunteers with inform consent to disclose this two necessary characteristics. Details are described in the Method section.
Recruitment	All subjects are healthy volunteers without known neurological disorders. No further exclusion criteria was applied to avoid selection bias. Before participating in the study, all subjects provided written consent. Details are described in the Method section.
Ethics oversight	The research protocols were approved by the Institute Review Board at both Columbia University and National Taiwan University Hospital.

Note that full information on the approval of the study protocol must also be provided in the manuscript.

Field-specific reporting

Please select the one below that is the best fit for your research. If you are not sure, read the appropriate sections before making your selection.

Life sciences Behavioural & social sciences Ecological, evolutionary & environmental sciences

For a reference copy of the document with all sections, see nature.com/documents/nr-reporting-summary-flat.pdf

Life sciences study design

All studies must disclose on these points even when the disclosure is negative.

Sample size	Due to the quantitative and precise nature of the readout, the sample size is predetermined by the statistical power based on the non-overlapping data points and a safe margin based on the successful rate of the surgical procedure. For paired experiments, the pre-estimated sample size is 5, based on Wilcoxon Signed Rank Test. For multiple comparison, the minimal sample size is 7, based on Kruskal-Wallis test. For parametric data, the pre-estimated minimal sample size is 15 based on One-way ANOVA. For More than expected data are all included, except those fulfilled the data exclusion criteria.
Data exclusions	The exclusion criteria is included in the "Tissue clearing and histological validation". Electrophysiological data were excluded in those mice with improper cannula placement or inadequate fluorescent expression.
Replication	Replication of experiments, if applied, are all described in the figure legend and show in the raw data spreadsheet.
Randomization	All experiments are self-controlled and randomization is not required.
Blinding	The experimental procedure and results are generated by automatic computer programs. No experimenter manipulation is involved and the results are essentially blinded to the experimenters.

Reporting for specific materials, systems and methods

We require information from authors about some types of materials, experimental systems and methods used in many studies. Here, indicate whether each material, system or method listed is relevant to your study. If you are not sure if a list item applies to your research, read the appropriate section before selecting a response.

Materials & experimental systems

n/a	<input checked="" type="checkbox"/> <input type="checkbox"/> Involved in the study
<input checked="" type="checkbox"/>	<input type="checkbox"/> Antibodies
<input checked="" type="checkbox"/>	<input type="checkbox"/> Eukaryotic cell lines
<input checked="" type="checkbox"/>	<input type="checkbox"/> Palaeontology and archaeology
<input type="checkbox"/>	<input checked="" type="checkbox"/> Animals and other organisms
<input checked="" type="checkbox"/>	<input type="checkbox"/> Clinical data
<input checked="" type="checkbox"/>	<input type="checkbox"/> Dual use research of concern
<input checked="" type="checkbox"/>	<input type="checkbox"/> Plants

Methods

n/a	<input checked="" type="checkbox"/> <input type="checkbox"/> Involved in the study
<input checked="" type="checkbox"/>	<input type="checkbox"/> ChIP-seq
<input checked="" type="checkbox"/>	<input type="checkbox"/> Flow cytometry
<input checked="" type="checkbox"/>	<input type="checkbox"/> MRI-based neuroimaging

Animals and other research organisms

Policy information about [studies involving animals](#); [ARRIVE guidelines](#) recommended for reporting animal research, and [Sex and Gender in Research](#)

Laboratory animals

We applied the following mouse strains for the experiments:
 C57B6/JNarl were used as wild-type mice.
 For DCN optogenetics: B6.Cg-Tg(Thy1-COP4/EYFP)9Gfng/J, Jackson Laboratory, No. 007615
 For optogenetic stimulation in the PCs, we crossed Calbindin-Cre mice (B6;129S-Calb1tm2.1(cre)Hze/J, Jackson Laboratory, No. 028532) with Ai32 mice (B6;129S-Gt(ROSA)26Sortm32(CAG-COP4*H134R/EYFP)Hze/J, Jackson Laboratory, No. 012569).
 Full details are included in the "Animals" section of the method, including the Jackson category number of all transgenic strains.

Wild animals

No wild-animals were used in this study.

Reporting on sex

Animal of both sex were used in all experiments. There are total 109 mice used for the whole study, including 56 male and 53 female mice. This study provided evidence of cross-individual uniformity, essentially meaning no sex differences in all tested profiles.

Field-collected samples

No field collected samples were used in the study.

Ethics oversight

All procedures were approved by the Institutional Animal Care and Use Committee (IACUC) of National Taiwan University (Protocol numbers: B201900034, B202000003, B202100150).

Note that full information on the approval of the study protocol must also be provided in the manuscript.

Plants

Seed stocks

N/A

Novel plant genotypes

N/A

Authentication

N/A